Journal Pre-proofs

Mathematical modeling accurately predicts the dynamics and scaling of nuclear growth in discrete cytoplasmic volumes

V. Leech, J.W. Hazel, J.C. Gatlin, A.E. Lindsay, A. Manhart

PII: S0022-5193(21)00355-6
DOI: https://doi.org/10.1016/j.jtbi.2021.110936
Reference: YJTBI 110936

To appear in: *Journal of Theoretical Biology*

Received Date: 22 July 2021
Accepted Date: 10 October 2021

Please cite this article as: V. Leech, J.W. Hazel, J.C. Gatlin, A.E. Lindsay, A. Manhart, Mathematical modeling accurately predicts the dynamics and scaling of nuclear growth in discrete cytoplasmic volumes, *Journal of Theoretical Biology* (2021), doi: https://doi.org/10.1016/j.jtbi.2021.110936

Mathematical modeling accurately predicts the dynamics and scaling of nuclear growth in discrete cytoplasmic volumes

V. Leech[a], J.W. Hazel[b,d], J.C. Gatlin[b,d], A.E. Lindsay[c], A. Manhart[a]

[a]*Dept. of Mathematics, University College London, London, WC1H 0AY, UK*
[b]*Dept. of Molecular Biology, U. Wyoming, Laramie, WY, 82071, USA*
[c]*Dept. of Applied and Computational Mathematics and Statistics, University of Notre Dame, South Bend, 46656, IN, USA*
[d]*Cell Division and Organization Group, Marine Biological laboratory, Woods Hole, 02543, MA, USA*

Abstract

Scaling of nuclear size with cell size has been observed in many species and cell types. In this work we formulate a modeling framework based on the limiting component hypothesis. We derive a family of spatio-temporal mathematical models for nuclear size determination based on different transport and growth mechanisms. We analyse model properties and use *in vitro* experimental data to identify the most probable mechanism. This suggests that nuclear volume scales with cell volume and that a nucleus controls its import rate as it grows. We further test the model by comparing to data of early frog development, where rapid cell divisions set the relevant time scales.

Keywords: Nuclear Growth, Partial differential equations, Free boundary problems

Acknowledgements: NSF support acknowledged under grants DMS-1815216 (AEL), DMS-2052636 (AEL, AM), DMS-2052640 (JCG). JCG acknowledges support under a Whitman center fellowship and from the National Xenopus Resource at the MBL.

1. Introduction

Scaling in biology concerns the question of how one quantity, e.g. the size of an organism, relates to another quantity, e.g. its life span. A famous example is Kleiber's law, which states that the metabolic rate of an animal scales to the 3/4 power of the animal's mass [20]. While a scaling law by itself merely states an observed relationship, if observed across many species or conditions, it can point towards fundamental design principles in nature. In this work, we are concerned with scaling at the cellular level, specifically scaling of the size of a cell and its nucleus. We will use mathematical modelling to understand observed scaling relationships as well the time dynamics that lead to them.

The nucleus is a critically important organelle in eukaryotic cells. Structurally it consists of a double lipid bilayer that physically separates the cell's genetic material from the rest of the cytoplasm. The transport of many proteins through nuclear pores is regulated resulting in a nucleoplasm that is compartmentalized and biochemically distinct from the cytoplasm. Nuclear size is known to correlate with amount of genetic material [2, 11], however experimental data suggests that the amount of genetic material is more likely to set a lower size limit, rather than determining the nuclear size [22, 35]. For many cell types it has been shown that the ratio between nuclear and cytoplasmic volume (called the karyoplasmic ratio) is typically constant [5, 16]. In fission yeast several ingenious experiments demonstrate convincingly that it is in fact components of the cytoplasm that control nuclear growth. Further it has been observed that it is the relative amount

Email addresses: vivienne.leech.16@ucl.ac.uk (V. Leech), jgatlin@uwyo.edu (J.C. Gatlin), a.lindsay@nd.edu (A.E. Lindsay), a.manhart@ucl.ac.uk (A. Manhart)

of cytoplasm that matters [24], i.e. that the position of nucleus within a cell matters. This suggests that transport from the cytoplasm to the nucleus is important and that cytoplasmic volume is a possible regulator of nuclear size. However, which cytoplasmic component or components regulate nuclear size is still being debated.

Several works suggest that it is in fact the availability of components of the nucleus that sets nuclear size: The inner nuclear membrane is lined with a meshwork of lamin intermediate filaments. It has been observed that Lamin depletion reduces nuclear size [25]. In [6] the authors show that the histone chaperone nucleoplasmin (Npm2), which binds core histones, affects nuclear scaling. It has also been shown that the transport between the cytoplasm and the nucleus plays an important role in setting nuclear size. In "open" division cell types [12], the nuclear membrane breaks down to allow the genetic material to be distributed between the two daughter cells. After division the nuclear membrane reforms and the nucleus expands again. This growth process required communication between the nucleus and the cytoplasm, which is mediated predominantly by nuclear pore complexes (NPCs). NPCs are large protein complexes that are inserted into the nuclear membrane [7] and act as gatekeepers for nuclear import and export. In [21] they show that if nuclear transport is affected, this impacts nuclear growth speed in Xenopus extracts. They suggest that there might be two scaling regimes: one where nuclear components are not limiting and nuclear size is mostly determined by nuclear import and cell cycle timing and one where nuclear components become limiting. We will explore both regimes with our model.

In general, mechanistic models explaining size scaling typically either suggest 1) a component-limiting mechanism, where the total amount of some component determines the final size or 2) a balancing-based mechanism, where two effects, e.g. import and export balance in equilibrium. In this work we focus on the first option, since the role of nuclear export in nuclear scaling is less clear: [19] observed that blocking nuclear export in budding yeast failed to affect nuclear size, while [24] observed it does increase nuclear size in fission yeast, suggesting mechanism might be dependent on the species. However, it is also possible that non-export dependent processes could play a role, such as nuclear membrane tension, osmotic effects, etc. Though not considered here, including these effects in the model and assessing their impact could be subject to future work.

In this work, we assume the existence of a cytoplasmic component that regulates nuclear size, without specifying its identity. This molecule could be either a component of the nucleus or its membrane, as well as a signal that causes nuclear growth through downstream effects. In the following we will refer to it simply as nuclear growth factor (NGF). While many scaling models focus on the steady state behaviour, the purpose of this work is to include the dynamics. We formulate, analyse and simulate a group of mathematical models that capture 1) the transport of the NGF through the cytoplasm, 2) its NPC dependent transport into the nucleus and 3) its effect on nuclear growth. In particular, the models capture both the dynamics and the final state behaviour of nuclear growth. The models use a common framework, that allows to test six different hypotheses concerning how the NGF affects nuclear growth and how NPC density on the nuclear surface changes in time. The aim is to have a modelling framework detailed enough to capture all relevant temporal and spatial scales, while being simple enough to be characterized by few parameters, allowing for parameter fitting as well as rapid simulation.

In Sec. 2 and Sec. 3 we introduce the models, consisting of partial-differential equations posed on a moving domain coupled to an ordinary differential equations model for nuclear growth. After discussing basic properties we use asymptotic analysis in Sec. 4 to derive a family of approximating models that hold in a certain parameter regime. We analyse their behaviour in Sec. 5. In Sec. 6 we test the model against two sets of experimental observations: Firstly, we use the nuclear growth model to test the six hypotheses against data of nuclear growth measured in *in vitro* cell-mimicking droplets, that do not divide. Secondly, we assess how well the model predictions compare to published observations about early frog development, where cells undergo a rapid series of reductive

divisions and the time scale of nuclear growth determines nuclear size. Finally, in Sec. 7 we discuss current model limitations and possible extensions.

2. Model Derivation and General Properties

To emphasise basic properties, we will start with an arbitrary cell and nuclear shape. Further simplifications will be done below in Sec. 3.

General set-up. To model the growth of the nucleus inside a cell, we pose an equation for the concentration of NGF. We do not specify its identity, but a potential candidate could be Npm2 (see Sec. 1). We assume the cell stays constant in size, but the nucleus can grow. If we denote by $\mathcal{C} \subset \mathbb{R}^3$ the inside of the cell and by $\mathcal{N}(t) \subset \mathcal{C}$ the inside of the nucleus, then the equation for the NGF concentration at time $t \geq 0$, $u(\mathbf{x}, t)$, will be posed on $\Omega(t) := \mathcal{C} \backslash \mathcal{N}(t)$. We assume no reactions involving the NGF happen inside the cytoplasm and that the NGF moves with flux $\mathbf{J}$, which can include diffusive and advective fluxes. The latter could be caused e.g. by transport along microtubules. The NGF cannot penetrate the cell membrane $\partial\mathcal{C}$. At the nuclear membrane $\partial\mathcal{N}(t)$, it is absorbed with absorption rate $\kappa > 0$, which is proportional to NPC density and can therefore depend on time (see discussion in Sec. 3). We assume that once inside the nucleus, the NGF cannot leave the nucleus and will lead to nuclear growth. This can be the case because the NGF is a component of the nucleus or its membrane.

Domain deformation. Our domain (the cytoplasm) $\Omega(t)$ will change as the nucleus grows. Hence we need to prescribe how material points move as a consequence. We denote the material point velocity by $\mathbf{v}$. In this model we focus on nuclear growth, consequently the domain shrinks over time. The cytoplasm consists of both fluid and immersed structures, such as proteins, organelles, fibres, etc. The fluid itself can move through the nuclear membrane by osmosis and we assume the fluid is incompressible. However, the immersed structures can not pass through the nuclear membrane and will be compressed as the nucleus grows. We assume that the NGF is mainly transported with the (incompressible fluid) and consequently the domain shrinkage due to nuclear growth will only have an effect on the NGF movement at the nuclear membrane, where it will be moved with the nuclear growth speed. In Appendix B we show a model that assumes a compressible cytoplasm.

The governing equations. Since we assume the cytoplasm is incompressible, we have $\mathbf{v} \equiv 0$ inside the domain $\Omega(t)$. In this case we obtain

$$\begin{aligned} &\partial_t u = -\nabla \cdot \mathbf{J}, \qquad \mathbf{x} \in \Omega(t) \\ &\mathbf{n} \cdot \mathbf{J} = 0 \qquad \mathbf{x} \in \partial\mathcal{C}, \\ &\mathbf{n} \cdot \mathbf{J} = \kappa u + \mathbf{n} \cdot (u\mathbf{v}) \qquad \mathbf{x} \in \partial\mathcal{N}(t), \end{aligned} \tag{1}$$

where $\mathbf{n}$ denotes the outward unit normal. If we assume the material point velocity at the nuclear membrane occurs normal to the nuclear membrane and with speed $\dot{R}$, we can replace it by $\mathbf{v} = -\mathbf{n}\dot{R}$ and the boundary condition at $\partial\mathcal{N}$ simplifies to

$$\mathbf{n} \cdot \mathbf{J} = \left(\kappa - \dot{R}\right) u \qquad \mathbf{x} \in \partial\mathcal{N}(t).$$

Total NGF balance. We denote by $U(t)$ the total amount of NGF in the cytoplasm at time t. By integrating (1) over the whole domain $\Omega(t)$ and using Reynold's transport theorem and the divergence theorem, we see that

$$\begin{aligned} \dot{U}(t) &= \frac{\mathrm{d}}{\mathrm{d}t} \int_{\Omega(t)} u(\mathbf{x}, t)\, \mathrm{d}V = \int_{\Omega(t)} \partial_t u \, \mathrm{d}V + \int_{\partial\Omega(t)} \mathbf{n} \cdot (u\mathbf{v}) \, \mathrm{d}\Gamma \\ &= -\kappa \int_{\partial\mathcal{N}(t)} u \, \mathrm{d}\Gamma. \end{aligned} \tag{2}$$

As expected, this shows that the total amount of NGF in the cytoplasm will decrease over time. Next, we need to model how the nucleus grows as a consequence of the amount of NGF it receives. We denote by $S(t)$ the amount of NGF that enters the nucleus per time. Since this equals the amount of NGF that left the cytoplasm per time, we have that $S(t) = -\dot{U}(t)$.

Nuclear growth. Nuclear growth happens as a consequence of the NGF reaching the nucleus. How absorbed NGF is translated into nuclear growth is the key scaling question. The following scenarios (or combinations of them) are possible: The amount of NGF received per time is proportional to

- G1 the change in nuclear *radius* per time. This would be the case if the NGF is a component of a linear structure inside the nucleus.
- G2 the change in nuclear *surface area* per time. For instance, if the NGF is a component of the nuclear membrane, this would be the case.
- G3 the change in nuclear *volume* per time. This could be the case if the NGF molecule consists of or affects components of the nucleoplasm.

Basic scaling relationships. If we denote by $\mathcal{Z}(t)$ either nuclear radius (G1), nuclear surface area (G2) or nuclear volume (G3), then the above considerations can be written as

$$\dot{\mathcal{Z}}(t) = \alpha S(t),$$

where $\alpha > 0$ is the proportionality constant that quantifies how one unit NGF is translated into one unit size (radius, area or volume). Noting that $S(t) = -\dot{U}(t)$, we can integrate the relationship $\dot{\mathcal{Z}}(t) = -\alpha \dot{U}(t)$ from zero to $t > 0$. Rearranging yields

$$U(t) = \frac{1}{\alpha}\left(\mathcal{Z}_l - \mathcal{Z}(t)\right), \quad \mathcal{Z}_l := \mathcal{Z}(0) + \alpha U_0, \tag{3}$$

where U_0 denotes the initial total amount of NGF and $\mathcal{Z}_l$ is defined as the limiting nuclear size reached if all the NGF is eventually absorbed into the nucleus, i.e. $U = 0$. In this case $\mathcal{Z}(t) \to \mathcal{Z}_l$ and we have a linear relationship between the final nuclear size and the total initial amount of NGF. Note that the final nuclear size is not a consequence of the balancing of different effects, rather it is the limiting size, when all the NGF has been absorbed. If we assume that $\mathcal{Z}(0) \approx 0$ and that the initial average concentration of NGF is the same in each cell, then we can express U_0 as $U_0 = \bar{u}|\mathcal{C}|$, where $|\mathcal{C}|$ is the volume of the cell and $\bar{u}$ is the initial average concentration of NGF in the cytoplasm. This yields the following scaling relationship

$$\mathcal{Z}_l = \alpha\, \bar{u}\, |\mathcal{C}|, \tag{4}$$

or, expressed in words

$$\text{final nuclear size} \propto \text{cell volume}$$

where *final nuclear size* can mean radius, surface area or volume. Hence, if we can measure the initial cell and nuclear size, then (4) gives a way to test the hypotheses C1-C3 for a dataset with a range of cell sizes and nuclear sizes. However, there are some notable limitations: Firstly, it requires having data on fully equilibrated nuclei and secondly, all dynamical information, i.e. *how* that steady state is reached, is not used. Next we make some simplifying assumptions allowing us to derive a model for nuclear growth that has the same basic scaling properties, but can be analysed on a deeper mathematical level.

3. Radially symmetric nuclear growth model.

The model in the above section was formulated for an arbitrary cell and nuclear shape, and arbitrary fluxes and material point velocity. To further analyse the model, we now make a number of assumptions. We assume a purely diffusive flux $\mathbf{J} = -D\nabla u$ with diffusion constant $D > 0$. Further, with regards to the geometry, we assume both the cell and the nucleus are concentric spheres with radii R_c and $R(t)$ respectively and radial symmetry is assumed for all involved quantities. As a consequence, the NGF concentration is now a function of the radial direction r and time t only, $u(r, t)$. Rewriting all operators in spherical coordinates, we can now simplify the equations.

Main Model. If the NGF is transported mainly with the incompressible components of the cytoplasm, we use (1), which simplifies to

$$\begin{aligned} &\partial_t u = D\frac{1}{r^2}\partial_r\left(r^2\partial_r u\right), \quad R(t) < r < R_c; \\ &D\partial_r u = 0, \quad r = R_c; \\ &D\partial_r u = \left(\kappa - \dot{R}\right)u, \quad r = R(t). \end{aligned} \tag{5}$$

Note that the boundary condition at $r = R(t)$ shows that if nuclear growth dominates absorption, i.e. $\dot{R} > \kappa$, then the gradient of u will be negative, since the NGF is being pushed outwards faster than it is being absorbed. Conversely if absorption dominates growth $\dot{R} < \kappa$, the gradient will be positive.

We supply given initial conditions: We set $R(0) = R_0 < R_c$. We always assume R_0 to be small, but positive (see discussion in Sec. 4.1). Further we set $u(r, 0) = w(r)$ and define the initial average concentration $\bar{u}$ by

$$\bar{u} = \frac{1}{|\Omega(0)|}\int_{\Omega(0)} w \,\mathrm{d}V = \frac{3}{R_c^3 - R_0^3}\int_{R_0}^{R_c} r^2 w(r)\,\mathrm{d}r. \tag{6}$$

The total NGF amount at time $t > 0$ is now given by

$$U(t) = \int_{\Omega(t)} u \,\mathrm{d}V = 4\pi\int_{R(t)}^{R_c} r^2 u(r,t)\,\mathrm{d}r$$

Nuclear growth. As before, we assume that the change in nuclear size (quantified by nuclear radius, surface area or volume) per time is proportional to the amount of NGF the nucleus receives per time, given by $S(t)$. In this radially symmetric setting we can simplify (2) and obtain

$$S(t) = -\dot{U}(t) = 4\pi\kappa R(t)^2 u(R(t), t).$$

We see that this is simply the NGF amount at the nuclear membrane $u(R(t), t)$, multiplied by the nuclear surface area $4\pi R(t)^2$ and the (potentially time dependent) absorption rate κ.

We denote by $A(t)$ and $V(t)$ the nuclear surface area and nuclear volume respectively and recapitulate the growth assumptions G1-G3 and corresponding scaling relationship results of Sec. 2. Here $V_c = \frac{4\pi}{3}R_c^3$ is the cell volume.

G1: $\dot{R}(t) = \alpha S(t)$ leading to $R_l = R_0 + \alpha U_0$. If $R_0 \approx 0$, we obtain $R_l = \alpha\bar{u}V_c$.

G2: $\dot{A}(t) = \alpha S(t)$ leading to $A_l = A_0 + \alpha U_0$. If $R_0 \approx 0$, we obtain $A_l = \alpha\bar{u}V_c$.

G3: $\dot{V}(t) = \alpha S(t)$ leading to $V_l = V_0 + \alpha U_0$. If $R_0 \approx 0$, we obtain $V_l = \alpha\bar{u}V_c$.

An important note is that in principle in this model the nucleus could reach cell size, which isn't meaningful biologically. To be specific and assuming R_0 is small this would happen if

$$1 < \begin{cases} \frac{4\pi\alpha\bar{u}R_c^2}{3} & \text{for G1} \\ \frac{\alpha\bar{u}R_c}{3} & \text{for G2} \\ \alpha\bar{u} & \text{for G3} \end{cases} \tag{7}$$

Biologically, this means that irrespective of $\alpha\bar{u}$, for both G1 and G2 large enough cells would lead to too large nuclei. Only for G3 is it possible to have cell-independent parameters $\alpha\bar{u}$ such that nuclei will never outgrow the cell for any cell size. Below in Sec. 5 we explore further what happens if the limiting conditions are violated. In real cells we of course do not expect nuclei to reach the size of the cell, however *in vitro* it might happen that the nucleus grows very large and that subsequently the cell is destroyed. This could be tested experimentally.

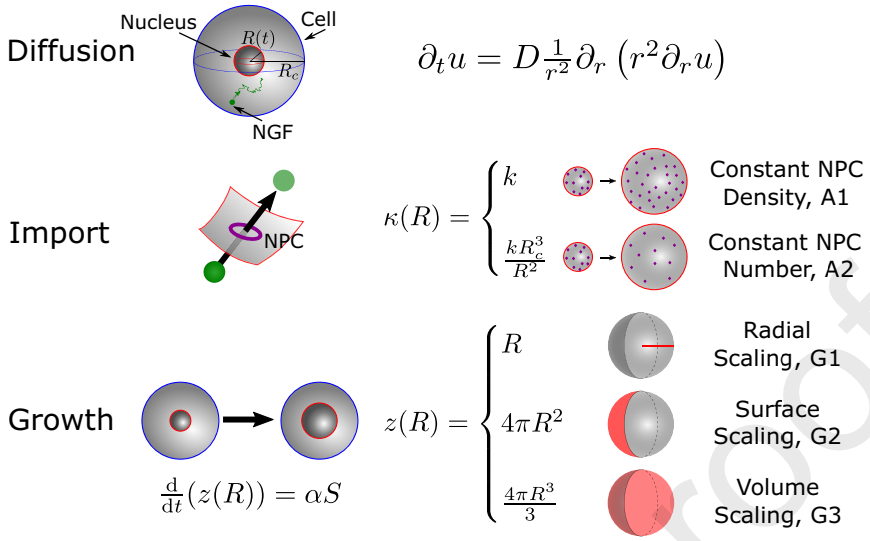

Figure 1: Summary of model components.

Absorption rate. From the derived scaling relationships we see that the final nuclear size is fully determined by the initial nuclear size, the initial amount of NGF and the "translation rate" α, which quantifies how one unit NGF is translated to nuclear growth. The absorption rate κ on the other hand sets the time scale for nuclear growth. Larger sized molecules are transported into the nucleus via nuclear pore complexes (NPCs) on the nuclear membrane.

The relationship between the absorption rate κ and NPC organization has been studied in the context where NPCs are small open pores and homogeneously spaced on the otherwise impermeable nuclear envelope. For individual NPC radius a_0, surface NPC coverage fraction f and small dimensionless parameter $\sigma = (a_0/R)$, it was shown in [23, 3] that

$$\kappa \sim \frac{D}{R}\frac{4f}{\pi\sigma}\left[1 - \frac{4}{\pi}\sqrt{f} + \frac{\sigma}{\pi}\log\left(\beta\sqrt{f}\right) + \mathcal{O}(\sigma^2)\right]^{-1}, \qquad \beta = 4e^{-1/2}. \tag{8}$$

For low NPC coverage fraction $f \ll 1$, the absorption rate κ is therefore proportional to the NPC surface density. The correction term $\sqrt{f}$ describes how flux competition between neighboring NPCs reduces the permeability of the membrane while the logarithmic term is a consequence of the spherical geometry of the nucleus.

In modelling of NPC dynamics during nuclear growth, we consider two options:

A1: As the nucleus grows, new NPCs are produced to keep the NPC surface density constant. This means that κ remains constant in time and we assume this constant to be global across different cells.

A2: The NPC number is constant and no new NPCs are produced (or destroyed) during nuclear growth. We assume the NPC number is determined by some component initially present in the cytoplasm, whose concentration is the same for different cells. This means that the NPC number is proportional to the size of the cell. Hence the NPC density (number of NPCs per surface area) is proportional to R_c^3 and decreases with nuclear surface area. Consequentially also κ is proportional to R_c^3 and decreases with nuclear surface area, i.e. quadratically in $R(t)$.

Summary of nuclear growth models. In total we examine six different models for nuclear growth as depicted in Fig. 1: All combinations of nuclear growth assumptions G1-G3 and NPC density assumptions A1, A2. Since the model equations (5) are formulated in terms of the nuclear radius, we use the formulas for the surface area and volume of a sphere, $A = 4\pi R^2$ and $V = \frac{4\pi}{3}R^3$, to reformulate the growth relationships in terms of the change in nuclear radius R. This yields

$$\frac{\mathrm{d}}{\mathrm{d}t}\left(z(R)\right) = 4\pi\alpha\kappa(R)R^2u(R,t), \qquad R(0) = R_0. \tag{9}$$

The constant α has units length per amount NGF for A1, length squared per amount NGF for A2 and length cubed per amount NGF for A3. The function $z(R)$ corresponds to the different measures of nuclear size: nuclear radius, nuclear area or nuclear volume and $\kappa(R)$ is determined by assumption A1,A2, i.e.

$$z(R) = \begin{cases} R & \text{for G1} \\ 4\pi R^2 & \text{for G2} \\ \frac{4\pi}{3}R^3 & \text{for G3} \end{cases}, \qquad \kappa(R) = \begin{cases} k & \text{for A1} \\ k\frac{R_c^3}{R^2} & \text{for A2,} \end{cases} \tag{10}$$

where $k > 0$ with units length per time for A1 and per time for A2. Equation (9) complements the NGF equation (5) by defining the dynamics of the free boundary.

4. Deriving Approximating Models

4.1. Non-dimensionalisation

To prepare the derivation of approximating models, we non-dimensionalise (5) and (9). We choose R_c as reference length, $t_r = \frac{R_c}{k}$ as reference time for A1 and $t_r = \frac{1}{k}$ as reference time for A2 and $\bar{u}$ as defined in (6) as reference concentration. Using tilde to denote dimensionless quantities, we define $\tilde{r} = r/R_c$, $\tilde{t} = t/t_r$, $\tilde{u}(\tilde{r},\tilde{t}) = u(r,t)/\bar{u}$, $\tilde{R}(\tilde{t}) = R(t)/R_c$, $\tilde{w}(\tilde{r}) = w(r)/\bar{u}$. Further we define the following non-dimensional parameters

$$r_0 = \frac{R_0}{R_c}, \quad \varepsilon = \begin{cases} \frac{R_c k}{D} & \text{for A1} \\ \frac{R_c^2 k}{D} & \text{for A2} \end{cases}, \quad a = \begin{cases} 4\pi\bar{u}\alpha R_c^2 & \text{for G1} \\ 4\pi\bar{u}\alpha R_c & \text{for G2} \\ 4\pi\bar{u}\alpha & \text{for G3.} \end{cases}$$

Note that since α and k have different units for G1-3 and A1, A2 respectively, a and ε are always non-dimensional.
We obtain the non-dimensional equations

$$\varepsilon\partial_{\tilde{t}}\tilde{u} = \frac{1}{\tilde{r}^2}\partial_{\tilde{r}}\left(\tilde{r}^2\partial_{\tilde{r}}\tilde{u}\right), \qquad \tilde{R} < \tilde{r} < 1 \tag{11a}$$

$$\partial_{\tilde{r}}\tilde{u} = 0, \qquad \tilde{r} = 1 \tag{11b}$$

$$\partial_{\tilde{r}}\tilde{u} = \varepsilon\left(\tilde{\kappa}(\tilde{R}) - \frac{\mathrm{d}\tilde{R}}{\mathrm{d}\tilde{t}}\right)\tilde{u}, \quad \tilde{r} = \tilde{R}, \tag{11c}$$

together with the nuclear growth equation

$$\frac{\mathrm{d}}{\mathrm{d}\tilde{t}}\left(\tilde{z}(\tilde{R})\right) = a\tilde{\kappa}(\tilde{R})\tilde{R}^2\tilde{u}(\tilde{R},\tilde{t}), \tag{12}$$

where $\tilde{z}(\tilde{R}) = z(\tilde{R})$ and $\tilde{\kappa}(\tilde{R}) = 1$ for A1 and $\tilde{\kappa}(\tilde{R}) = 1/\tilde{R}^2$ for A2. The initial conditions are given by

$$\tilde{R}(0) = r_0, \quad \tilde{u}(\tilde{r},0) = \tilde{w}(\tilde{r}), \quad \text{with} \quad \frac{3}{1-r_0^3}\int_{r_0}^{1}\tilde{r}^2\tilde{w}(\tilde{r})\,\mathrm{d}\tilde{r} = 1. \tag{13}$$

Non-dimensional quantities. The non-dimensional quantities ε, r_0 and a characterise the system's behaviour. Let us interpret them one by one: r_0 is simply the ratio of the initial nuclear radius to the cell radius. While we assume quasi *de nuovo* nuclear growth, $r_0 = 0$ can lead to problems, since a zero-surface nucleus cannot absorb any NGF. Therefore we keep r_0 small, but positive. Next, a is the ratio of the nuclear size gain upon total NGF absorption, and the cell size. For instance for G1 it is proportional to the ratio between $\alpha\bar{u}V_c$ (total nuclear radius gained for *de nuovo* growth) and R_c (cell radius). Hence it quantifies how efficiently NGF is translated into size. Finally, ε compares the speed at which diffusion carries the NGF across the cell, D/R_c, to the speed at which it is absorbed. Since diffusive transport acts to distribute the NGF equally in the cell, ε quantifies the spatial variation of NGF. We will discuss the order of magnitude for ε below after parameter fitting, but at least for small cells, ε will be small. Therefore we derive a simplified model that approximates the full dynamics for $\varepsilon \ll 1$.

4.2. Approximating Models

To derive approximating models, we wish to solve (11), (12) subject to (13) in the limit as $\varepsilon \to 0$. The solution is developed in terms of the regular expansion for $\tilde{u}(\tilde{r}, \tilde{t})$ and $\tilde{R}(\tilde{t})$,

$$\tilde{u} = \tilde{u}^0 + \varepsilon\tilde{u}^1 + \mathcal{O}(\varepsilon^2), \qquad \tilde{R} = \tilde{R}^0 + \varepsilon\tilde{R}^1 + \mathcal{O}(\varepsilon^2). \tag{14}$$

It is convenient to introduce $\tilde{W}(\tilde{R}^0) = (1-(\tilde{R}^0)^3)/3$, which is a measure of the cytoplasmic volume. Further we define a non-dimensional version of the total NGF amount $\tilde{U} = \int_{\tilde{R}}^1 \tilde{r}^2\tilde{u}\,\mathrm{d}\tilde{r}$ and expand it as $\tilde{U} = \tilde{U}^0 + \varepsilon\tilde{U}^1 + \mathcal{O}(\varepsilon^2)$, giving

$$\tilde{U}^0 = \int_{\tilde{R}^0}^1 \tilde{r}^2\tilde{u}^0(\tilde{r}, \tilde{t})\,\mathrm{d}\tilde{r}, \qquad \tilde{U}^1 = \int_{\tilde{R}^0}^1 \tilde{r}^2\tilde{u}^1(\tilde{r}, \tilde{t})\,\mathrm{d}\tilde{r} - \tilde{R}^1(\tilde{R}^0)^2\tilde{u}^0(\tilde{R}^0, \tilde{t}).$$

The second term in $\tilde{U}^1$ stems from the fact that in the definition of $\tilde{U}(t)$, the lower integral boundary depends on ε. In the following, we present only results with calculation details found in Appendix C.

The well-mixed model: The limit $\varepsilon \to 0$. Taking the limit $\varepsilon \to 0$ we find that the NGF concentration is spatially constant $\tilde{u}^0(\tilde{r}, \tilde{t}) = \tilde{u}^0(\tilde{t})$. Its dynamics are coupled to $\tilde{R}^0$ by

$$\frac{\mathrm{d}\tilde{u}^0}{\mathrm{d}\tilde{t}} = -\frac{1}{\tilde{W}}\tilde{u}^0\left(\tilde{R}^0\right)^2\left(\tilde{\kappa}(\tilde{R}^0) - \dot{\tilde{R}}^0\right), \quad \tilde{u}^0(0) = 1; \tag{15a}$$

$$\frac{\mathrm{d}}{\mathrm{d}\tilde{t}}\left(\tilde{z}(\tilde{R}^0)\right) = a\tilde{\kappa}(\tilde{R}^0)(\tilde{R}^0)^2\tilde{u}^0, \qquad \tilde{R}^0(0) = r_0. \tag{15b}$$

Note that the fact that nuclear growth is proportional to the amount of NGF lost in the cytoplasm manifests itself in the relation

$$\frac{\mathrm{d}}{\mathrm{d}\tilde{t}}\left(\tilde{z}(\tilde{R}^0)\right) = -a\frac{\mathrm{d}\tilde{U}^0}{\mathrm{d}\tilde{t}}. \tag{16}$$

In Sec. 5. we will capitalise on this and analyse system (15) in more depth. Note that exactly the same system is obtained if one assumes a compressible cytoplasm with an arbitrary continuous material point velocity (see Appendix B), showing that (15) approximates a wide range of models.

The approximate-spatial model: The order ε correction. The next higher order approximation, which captures spatial variations of the NGF, is given by

$$\tilde{u}^1(\tilde{r}, \tilde{t}) = \frac{\mathrm{d}\tilde{u}^0}{\mathrm{d}\tilde{t}}\left(g(\tilde{r}) - \frac{1}{\tilde{W}}\int_{\tilde{R}^0}^1 s^2 g(s)\,\mathrm{d}s\right) + \frac{1}{\tilde{W}}\left(\tilde{U}^1 + \tilde{R}^1(\tilde{R}^0)^2\tilde{u}^0\right),$$

where the profile g characterizing the spatial dependence, is given by

$$g(\tilde{r}) = \frac{2 + \tilde{r}^3}{6\tilde{r}}.$$

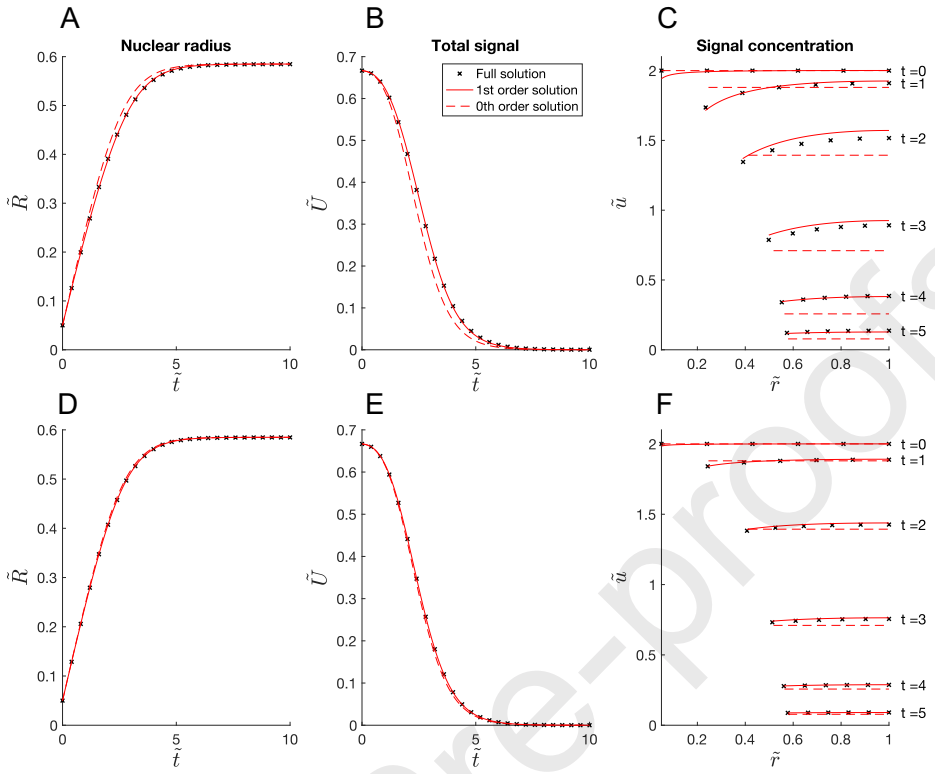

Figure 2: Comparison of the zeroth (red-dashed) and first order (red-solid) asymptotic solution with the full solution (black stars) for $\varepsilon = 0.8$ (A-C) and $\varepsilon = 0.2$ (D-F). A and D: A plot of the non-dimensional nuclear radius against time. B and E: plot of the non-dimensional total NGF against time. C and F: profiles of the non-dimensional NGF concentration against space for different time values. Other parameters are: $t \in [0, 10]$, $R_0 = 0.05$, $a = 0.4\pi$, $k = 15$ and $u_0 = 2$. Refer to Appendix D for a note on the initial conditions

The two time dependent quantities $\tilde{U}^1$ and $\tilde{R}^1$ fulfil

$$\frac{\mathrm{d}\tilde{U}^1}{\mathrm{d}\tilde{t}} = -\left[\tilde{\kappa}'\tilde{R}^1(\tilde{R}^0)^2\tilde{u}^0 + \tilde{\kappa}\tilde{u}^1(\tilde{R}^0)^2 + 2\tilde{\kappa}\tilde{R}^0\tilde{R}^1\tilde{u}^0\right]|_{\tilde{r}=\tilde{R}^0}, \quad \tilde{U}^1(0) = 0 \tag{17a}$$

$$\frac{\mathrm{d}}{\mathrm{d}\tilde{t}}\left(\tilde{z}'(\tilde{R}^0)\tilde{R}^1\right) = -a\frac{\mathrm{d}\tilde{U}^1}{\mathrm{d}\tilde{t}}, \qquad \tilde{R}^1(0) = 0. \tag{17b}$$

The shape function g, which corresponds to the spherical Green's function of the Laplacian, shows that the NGF profile is a monotone function in $\tilde{r}$. If $\frac{\mathrm{d}\tilde{u}^0}{\mathrm{d}\tilde{t}} < 0$ (i.e. nuclear growth is slow compared to NGF absorption), it takes its minimum at $\tilde{r} = \tilde{R}^0$ and its maximum at $\tilde{r} = 1$ and vice versa if $\frac{\mathrm{d}\tilde{u}^0}{\mathrm{d}\tilde{t}} < 0$. This is consistent with our intuition, since absorption leads to a local loss of NGF, while growth pushes the NGF into the cytoplasm, leading to an accumulation near the nuclear boundary.

4.3. Comparing the Approximate Model with the Full Model

One could prove a formal convergence result for $\varepsilon \to 0$ for the asymptotic approximations, however this is not the focus of this work. Instead we verify the asymptotic solutions numerically by comparing them to the solution to the non-dimensional full PDE model given by (11) and (12). For details on the numerical method to solve the full PDE model, see Appendix D. Fig. 2A and D show the non-dimensional nuclear radius $\tilde{R}$, Fig. 2B and E the non-dimensional total NGF concentration $\tilde{U}$ as functions of time. Fig. 2C and F show the spatial dependence of

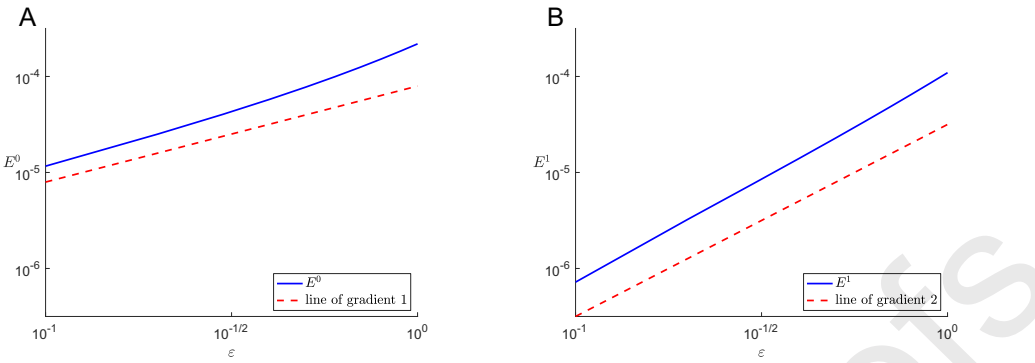

Figure 3: Error behaviour of the approximating solutions. Graphs showing plots of E^0 (A) and E^1 (B), given by (18) (solid-blue), against ε. Red-dashed lines are for comparison and have gradients 1 (A) and 2 (B).

the non-dimensional NGF concentration $\tilde{u}$ for different time values. As expected, the graphs show that the first order asymptotic approximation is a better approximation of the full solution than zeroth order approximation, and as ε gets smaller this approximation gets better overall.

Next we examine the residual error between the full and the approximate non-dimensional solution. To define a suitable norm, we have to be careful, since the different solutions might not be defined on the same $\tilde{r}$-interval. A natural choice of inner product for functions given in spherical coordinates is the L^2-norm with weight r^2, since it is equivalent to the L^2-inner product for functions given in Cartesian coordinates. However, the full solution $\tilde{u}(\tilde{r},\tilde{t})$ is defined for $\tilde{r} \in \left[\tilde{R}(\tilde{t}),1\right]$, whereas both its approximations are defined on $\tilde{r} \in \left[\tilde{R}^0(\tilde{t}),1\right]$. To ensure all solutions are defined in a common functional space, we extend all functions to $\tilde{r} \in [0,1]$ by 0 whenever $\tilde{r}$ is outside their original domain.

Hence we now define an inner product for any two functions $\tilde{u}(\tilde{r},\tilde{t})$ and $\tilde{v}(\tilde{r},\tilde{t})$ defined at a fixed time $\tilde{t}$ and on some $\tilde{r}$-interval contained in $[0,1]$ by

$$\langle \tilde{u},\tilde{v}\rangle = \int_0^1 \tilde{r}^2 \tilde{u}_c\, \tilde{v}_c \mathrm{d}\tilde{r},$$

where lowercase c denotes their continuations onto $[0,1]$. This inner product induces a norm by defining $||\tilde{u}|| = \sqrt{\langle \tilde{u},\tilde{u}\rangle}$. For a fixed time T, we define the error between the full solution and its approximations by

$$E^0 := ||\tilde{u}(r,T) - \tilde{u}^0(T)||, \tag{18a}$$
$$E^1 := ||\tilde{u}(r,T) - (\tilde{u}^0(T) + \varepsilon\tilde{u}^1(r,T))||, \tag{18b}$$

where $\tilde{u}$ is the full solution, $\tilde{u}^0$ is the zeroth order asymptotic solution, and $\tilde{u}^0 + \varepsilon\tilde{u}^1$ is the first order asymptotic solution. To verify numerically that $E^0 \leq C_0\varepsilon$ and that $E^1 \leq C_1\varepsilon^2$ for some ε-independent constants C_0 and C_1, we use a log-log plot of the error against ε. Inspecting the gradient of the resulting line in Fig. 3 indicates that the error behaves as expected.

5. Properties of the Well-mixed Models

In Sec. 4 we derived approximate equations for the nuclear growth and NGF dynamics for small ε. In this section we will discuss the main properties of the well-mixed model, i.e. the 0-th order approximation obtained for $\varepsilon \to 0$. We revert to variables with dimensions and, for ease of

notation, drop the superscript 0 for all variables. This means in the following $u(t)$ denotes the (spatially constant) NGF concentration and $R(t)$ the nuclear radius. The equations then read

$$\frac{\mathrm{d}u}{\mathrm{d}t} = -\frac{3uR^2}{R_c^3 - R^3}\left(\kappa(R) - \dot{R}\right), \quad u(0) = \bar{u} \tag{19a}$$

$$\frac{\mathrm{d}}{\mathrm{d}t}z(R) = 4\pi\alpha\kappa(R)R^2u, \qquad R(0) = R_0, \tag{19b}$$

where $\kappa(R)$ and $z(R)$ are given by (10).

This constitutes a system of two nonlinear ODEs. Note that if $R(t) \to R_c$ the denominator of (19a) tends to infinity. In fact we can further simplify this system. To see this, it is helpful to consider the total NGF in the cytoplasm $U(t)$ (to be precise, this is the 0-order contribution to the total NGF for the full system). For a spatially constant concentration, $U(t)$ is obtained by multiplying the NGF concentration $u(t)$ by the volume of the cytoplasm, giving

$$U(t) = \frac{4\pi}{3}u(t)\left(R_c^3 - R(t)^3\right). \tag{20}$$

Now we can capitalize on the relationships stated in (16) and also introduced in Sec. 2.

$$\textbf{G1:} \quad \dot{R} = -\alpha\dot{U}, \qquad \textbf{G2:} \quad \dot{A} = -\alpha\dot{U}, \qquad \textbf{G3:} \quad \dot{V} = -\alpha\dot{U}. \tag{21}$$

where $A(t) = 4\pi R(t)^2$ is the nuclear surface area and $V(t) = \frac{4\pi}{3}R(t)^3$ is the nuclear volume. Similar to what was done in Sec. 2, we can integrate these relationships from 0 to time t and solve for $U(t)$. This gives the following relationships, which are analogous to (3), but formulated in terms of radii,

$$\begin{aligned}
&\textbf{G1:} \quad U(t) = \frac{1}{\alpha}\left(R_l - R(t)\right), && R_l := R_0 + \alpha U_0, \\
&\textbf{G2:} \quad U(t) = \frac{4\pi}{\alpha}\left(R_l^2 - R(t)^2\right), && R_l^2 := R_0^2 + \frac{\alpha}{4\pi}U_0, \\
&\textbf{G3:} \quad U(t) = \frac{4\pi}{3\alpha}\left(R_l^3 - R(t)^3\right), && R_l^3 := R_0^3 + \frac{3\alpha}{4\pi}U_0.
\end{aligned} \tag{22}$$

The constant U_0 is the initial total NGF given by $U_0 = \frac{4\pi}{3}\bar{u}(R_c^3 - R_0^3)$ and the constant R_l represents the nuclear radius obtained if all the NGF has been absorbed into the nucleus, i.e. if $U = 0$. We will discuss below for which parameter regimes this happens.

If we now use (20), we can obtain $u(t)$ as a function of $R(t)$, which simplifies (19) to

$$\begin{aligned}
&\textbf{G1:} \quad \dot{R} = 3\kappa(R)\frac{R^2\left(R_l - R\right)}{R_c^3 - R^3}, && R_l = R_0 + \alpha U_0, && R(0) = R_0, \\
&\textbf{G2:} \quad \dot{R} = \frac{3\kappa(R)}{2}\frac{R\left(R_l^2 - R^2\right)}{R_c^3 - R^3}, && R_l^2 = R_0^2 + \frac{\alpha}{4\pi}U_0, && R(0) = R_0, \\
&\textbf{G3:} \quad \dot{R} = \kappa(R)\frac{R_l^3 - R^3}{R_c^3 - R^3}, && R_l^3 = R_0^3 + \frac{3\alpha}{4\pi}U_0, && R(0) = R_0.
\end{aligned} \tag{23}$$

Now each model G1-G3 is represented by a single nonlinear, autonomous ODE. However, note the initial nuclear radius R_0 and NGF concentration U_0 enter via the constant R_l.

Limiting behaviour. For each model we have two regions with different behaviour, depending on whether $R_l < R_c$ or $R_l > R_c$. These conditions are equivalent to those stated in (7) for the full, radially symmetric model. However, now we can analyse the behaviour in more depth. In Fig. 4, left column we plot the solution trajectories lying on the curves given by (22) in (U, R)-space for

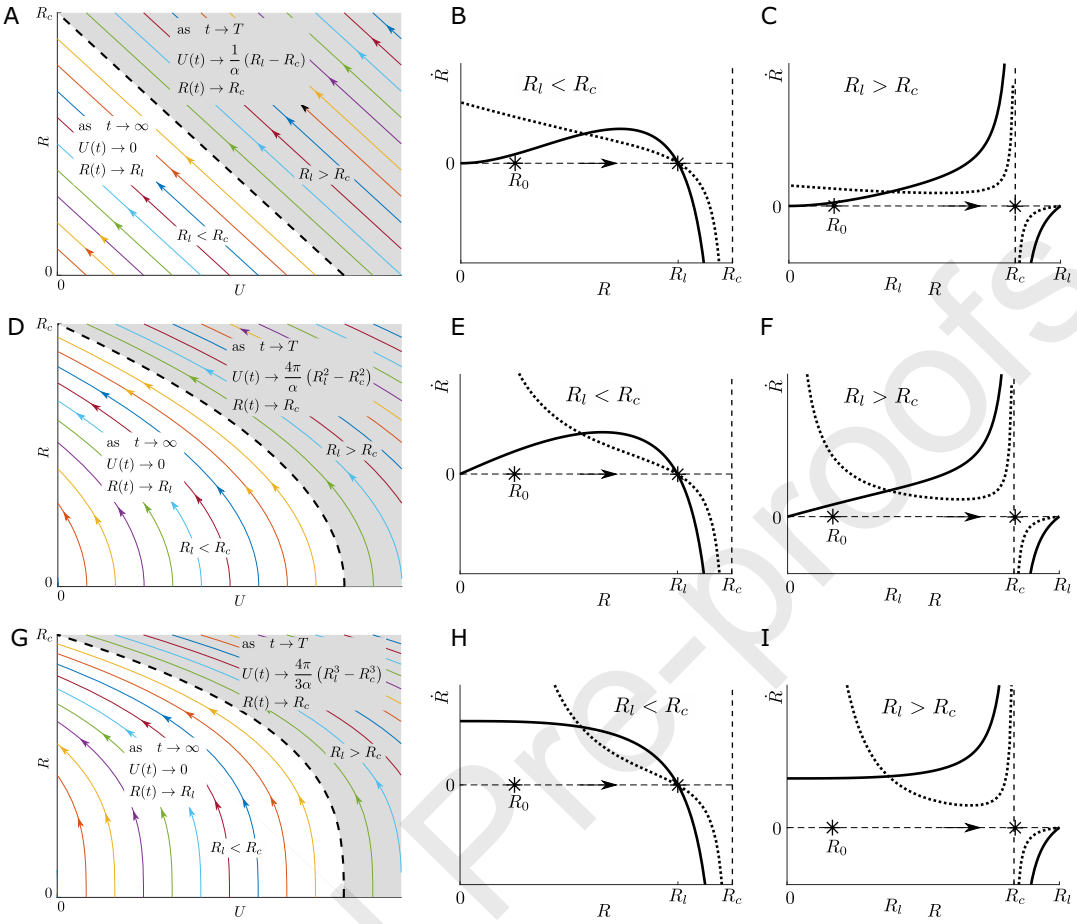

Figure 4: Left column: Dynamics in (U, R)-space for G1 (A), G2 (D) and G3 (G). Colored lines are the curves given by (22) for various initial conditions. Arrows indicate the direction in which the solution trajectories $t \mapsto (R(t), U(t))$ move on these curves. The white and shaded regions mark the parameter regime where $R_l < R_c$ and $R_l > R_c$ respectively. Middle and right columns depict the right-hand-sides of (23) as functions of R for $R_l < R_c$ (middle column) and $R_l > R_c$ (right column) for G1-G3. Solid curves refer to constant NPC density, dotted curves to constant NPC number, stars mark initial and final nuclear radii and the arrow marks the direction of the dynamics.

each of the growth assumptions G1-3. To capture the time dynamics along those curves we plot the right-hands-sides of (23) as functions of R in Fig. 4, middle and right column.

If $R_l < R_c$, then $R(t) \to R_l$ as $t \to \infty$ (white region in Fig. 4, left column). In this case all NGF is absorbed into the nucleus and $U(t) \to 0$ as $t \to \infty$. The final nuclear radius is smaller than the cell radius R_c. If $R_l > R_c$ then $R(t) \to R_c$ as $t \to T$, where T is a finite time. This time T can be evaluated explicitly, e.g. for G1 it is given by

$$T = \frac{1}{3} \int_{R_0}^{R_c} \frac{R_c^3 - R^3}{\kappa(R) R^2 (R_l - R)} \, \mathrm{d}R,$$

which is finite for $R_l > R_c$. Similar expressions can be obtained for G2 and G3 by separating variables and integrating (23). In this case the nucleus grows to cell size in finite time (shaded region in Fig. 4, left column). At this time there will be a leftover amount of NGF in the cytoplasm (given by replacing R by R_c in (22)), whose volume has shrunk to zero. Note that the concentration u tends to infinity in this case. As noted previously, $\kappa(R)$ does not affect the final nuclear size, only the time scale it takes to get there, which we will discuss next.

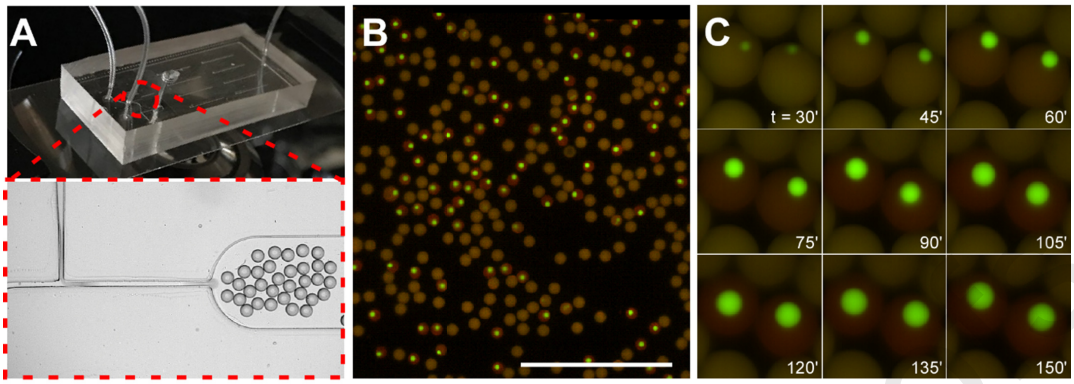

Figure 5: Nuclear growth in cell-free droplets of Xenopus laevis egg extract. A. Upper image shows a typical t-junction microfluidic device mounted on the stage of an inverted microscope. The two tubes at the lower left are inlets, with one carrying extract and the other oil. The tube at the upper right is the outlet. The lower panel shows a single frame of a transmitted light time-lapse of droplet formation in a t-junction device. Droplets can be seen entering the reservoir at the right. B. A stitched low-power image of droplets within the imaging reservoir of a PDMS device at some time $t > 90$min after encapsulation. Extract was spiked with a red fluorescent marker for microtubules and our green recombinant GFP-NLS probe. Image montage in C shows nuclear growth and GFP-NLS import as a function of time for two 70µm diameter droplets in a representative experiment.

Time scale of growth. As introduced in Sec. 3 we examine two models for the absorption rate κ, $\kappa \equiv k$ (constant NPC density) or $\kappa = \frac{kR_c^3}{R^2}$ (constant NPC number). The constant κ has units of speed (length per time) and sets the speed of nuclear growth. Its (potential) dependence on nuclear size via R influences how the absorption speed and hence growth speed changes over time. In the following discussion we focus on the biologically more relevant regime $R_l < R_c$. For constant NPC density (solid lines in Fig. 4, middle and right column) G1 and G2 predict $\dot{R} \to 0$ as $R_0 \to 0$. The nuclear growth rates then increase as the nucleus grows (quadratically in R for G1 and linearly in R for G2) and decrease as the nucleus approaches its final size R_l. G3, on the other hand, predicts that nuclear growth starts with a positive growth rate which stays approximately constant initially, but decreases over time. For constant NPC number (dotted lines in Fig. 4, middle and right column), κ declines as the nucleus grows, since there are fewer NPCs per surface area. Consequently we have a decline in nuclear growth rates in all cases, notably G2 and G3 predict very fast initial nuclear growth ($\dot{R} \to \infty$ as $R_0 \to 0$). We will examine this further below when we compare to experimental data.

6. Comparing model predictions to experimental data

In this section we demonstrate how we can use the derived models to understand biological data and gain biological insights. In the first part we use experimentally measured *in vitro* data of nuclear growth and focus on the following biological questions: Which scaling assumptions G1, G2 or G3 best explains the data? Which assumption about NPC dynamics A1, A2 explains the data the best? We will mainly use both the well-mixed and the approximate spatial model. Those have the advantage that they are much quicker to evaluate numerically compared to the full free boundary problem. This is helpful for data fitting, where we have to solve the system many times. In the second part we apply the model to early development in frog embryos, where cell divisions happen quickly which puts more importance on the time scale of nuclear growth. Since cells are very big initially, we use the full free boundary model.

6.1. Nuclear scaling in Xenopus extract.

Experimental data. To obtain information about *de novo* nuclear growth we used an in vitro model system that afforded exquisite control of "cell" size. (Fig. 5) Effectively, microfluidic-based

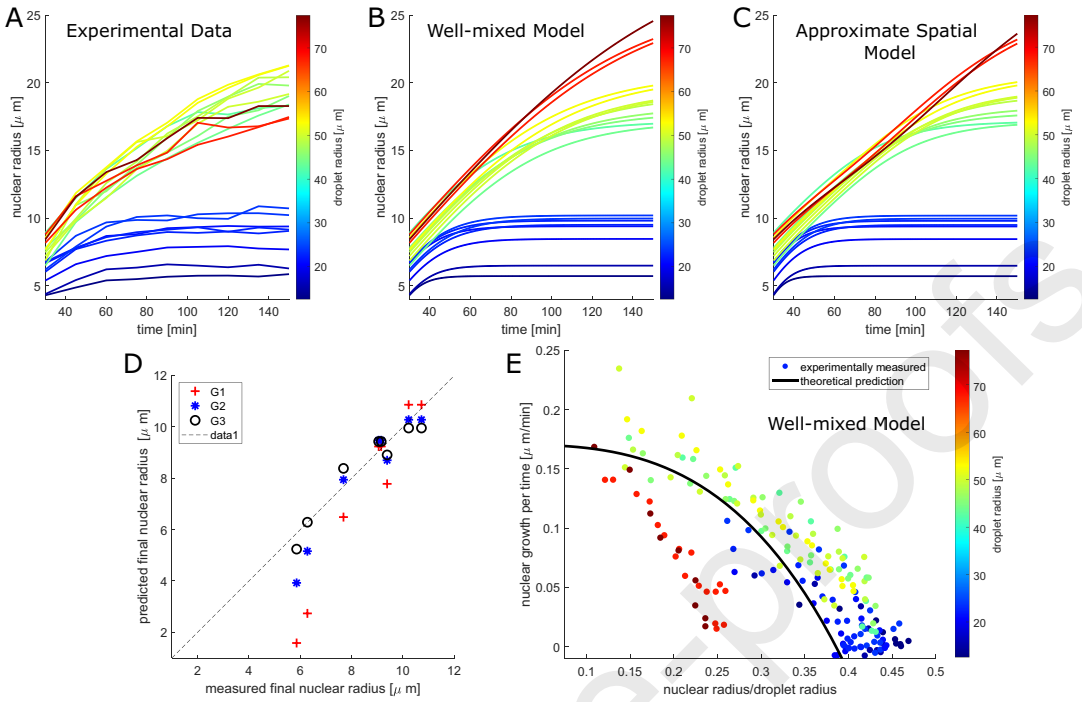

Figure 6: Comparing model predictions to measurements. A. Experimentally measured nuclear radii over time. Each line represents the average obtained from several droplets of similar size (line color indicates droplet radius), see Appendix A and Appendix E for more details. B. Simulation results for the G3-A1 well-mixed model using the identified best parameters $\alpha\bar{u} = 0.057$ and $k = 2.98\mu\text{m/min}$. C. Simulation results for the G3-A1 approximate spatial model using the identified best parameters $\alpha\bar{u} = 0.057$, $k = 4.44\mu\text{m/min}$ and $D = 72.8\mu\text{m}^2/\text{min}$. D. Using final state data of small droplets only, shown are the best fit results for G1 ($\alpha\bar{u} = 1.9410^{-4}/\mu\text{m}^2$), G2 ($\alpha\bar{u} = 0.237/\mu\text{m}$) and G3 ($\alpha\bar{u} = 0.0737$) obtained. E. Comparing the theoretical prediction for $\dot{R}$ of the G3-A1 model to the obtained measurements. Color represents droplet radius.

devices were used to encapsulate cell-free extracts derived from Xenopus laevis eggs into monodisperse droplets. Stochastic encapsulation of demembranated X. laevis sperm nuclei ensured that some droplets contained chromatin and would ultimately generate interphase nuclei. These cell-mimicking droplets are spherical, do not change in size over time, and initially contain no formed nucleus. A small recombinant protein containing GFP (green fluorescent protein) fused a nuclear localization signal was used to facilitate nuclear labeling and subsequent imaging using time-lapse, spinning-disk confocal microscopy (see Appendix A). Changes in nuclear size were monitored and measured over time and these data were collected for droplets of different sizes, see Fig. 6A. Each line represents nuclear radius data averaged over several droplets of similar size. We have included the full experimental data including standard deviations for each droplet size in Appendix E. For each of the 20 droplet sizes we obtained data from 9 time steps (every 15min). We focus on two groups: Small droplets (droplet radius 10-25μm) in which nuclei size equilibrates over the time course of the experiments, and large droplets (droplet radius 40-80μm), for which nuclei are still growing at the end of the experiment. In fact, we could not obtain data of the equilibrium sizes of nuclei in the large droplets, since nuclei became unstable when growing too large. Due to the controlled nature of the experiment, this is an ideal testing ground for the predictions of the spherically symmetric nuclear growth model. In the following, we denote by $\hat{R}_{i,j}$ the experimentally measured nuclear radius for a droplet size indexed by $j = 1, \ldots, N_D$, where $N_D = 20$ is the number of droplets and measured at a time point indexed by $i = 1, \ldots, N_T$, where $N_T = 9$ is the number of time points. Throughout this section we use the mean relative error (see definition below) to asses the match between simulation results and experimental measurements. We will always give

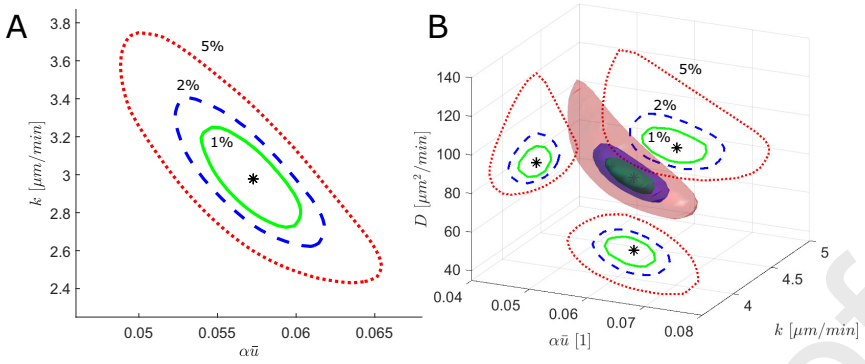

Figure 7: Parameter sensitivity. A. Shown are level sets of the error between the G3-A1 well-mixed model prediction and the experimental data for plus 1% of the minimal error (solid green), plus 2% of the minimal error (dashed blue) and plus 5% of the minimal error (dotted red). B. As in A, but using the G3-A1 approximate spatial model. Shown are the corresponding isosurfaces and their projections.

the relative error as percent deviation. Using the mean absolute error leads to slightly different, but qualitatively equivalent results.

Final state data gives only limited insights. We start by focusing on the equilibrated nuclear size, disregarding any dynamical information. Hence we only use the final time nuclear size measurements of the small droplets. We use the scaling relationship stated in (4) applied to the spherically symmetric case (also discussed in Sec. 2 and Sec. 3), reformulated in terms of the final nuclear radius R_l, yielding

$$R_l = \frac{4\pi\alpha\bar{u}}{3} R_c^3 \quad \text{(G1)}, \qquad R_l = \left(\frac{\alpha\bar{u}}{3}\right)^{\frac{1}{2}} R_c^{\frac{3}{2}} \quad \text{(G2)}, \qquad R_l = (\alpha\bar{u})^{\frac{1}{3}} R_c \quad \text{(G3)}.$$

For each scaling assumption, we find the best parameter $p = \alpha\bar{u}$ by minimizing the average relative error between predicted and measured final nuclear size

$$E_l(p) = \frac{1}{N_{D_s}} \sum_{j=1}^{N_{D_s}} \frac{|R_{l,j}(p) - \hat{R}_{N_T,j}|}{\hat{R}_{N_T,j}},$$

where the sum is only taken over the $N_{D_s} = 8$ small droplets and $R_{l,j}(p)$ denotes the predicted final nuclear size for a droplet whose radius R_c is the same as that with index j.

Fig. 6D shows the resulting best predictions for each model. The errors and best parameters are $E_l = 21.6\%$ at $\alpha\bar{u} = 1.93 \times 10^{-4}/\mu\text{m}^2$ for G1, $E_l = 9.3\%$ at $\alpha\bar{u} = 0.024/\mu\text{m}$ for G2 and $E_l = 5.2\%$ at $\alpha\bar{u} = 0.074$ for G3. We see that the error is minimal for scaling assumptions G3. However, given the low number of measurements, the difference in error to G2 does not give a lot of confidence in this result. Since we were restricted to using only final state data of equilibrated nuclei, we were only able to use less than 5% of the available data. Finally, no information about the dynamics of nuclear growth and the question about NPC density behaviour was gained.

The well-mixed model identifies G3-A1 as best model. Next we use the full dynamic experimental data to compare to the well-mixed model derived in Sec. 4 and analysed in Sec. 5. For each droplet size we solve (23) using R_c as the measured droplet radius and R_0 as the measured nuclear radius at the first time point. Hence we now have to fit two parameters, $\mathbf{p} = (\alpha\bar{u}, k)$ which we assume to be constant across different droplet sizes. We define the mean relative error

$$E(\mathbf{p}) = \frac{1}{N_D N_T} \sum_{j=1}^{N_D} \sum_{i=1}^{N_T} \frac{|R_{i,j}(\mathbf{p}) - \hat{R}_{i,j}|}{\hat{R}_{i,j}},$$

	A1			A2		
	error	$\alpha\bar{u}$	k	error	$\alpha\bar{u}$	k
G1	16.7%	$9.44 \times 10^{-5}/\mu m^2$	0.63μm/min	24.6%	$7.23 \times 10^{-6}/\mu m^2$	0.0260/min
G2	8.7%	0.0135/μm	1.80μm/min	16.5%	0.0280/μm	1.00×10^{-3}/min
G3	**6.3**%	0.0573	2.98μm/min	10.9%	2.43	6.94×10^{-5}/min

Table 1: Fitting results for the well-mixed model. Shown are the minimal average relative error obtained for each combination of hypotheses (G1-G3, A1,A2) and the corresponding identified parameters.

where $R_{i,j}(\mathbf{p})$ is the simulated nuclear radius at time point i for a droplet with the same droplet radius as droplet j. Tab. 1 summarizes the results and Fig. 6B shows the simulated nuclear growth. We see that the smallest error is produced by scaling assumption G3 together with NPC assumption A1 (which we will call the G3-A1 model), where the average deviation between predicted nuclear radius and measured nuclear radius is less than 6.5%. Hypothesis G3, which assumes that the amount of NGF absorbed is proportional to gain in nuclear volume, was already suggested by the analysis of the equilibrium data of the small droplets, but is now confirmed using the much larger dataset. Further, this is also in line with the frequently made observation across many organisms, that cells maintain a constant nuclear volume to cell volume ratio [5, 16]. Hypothesis A1 suggests that NPC surface density is in fact controlled, hence new NPCs are being incorporated into the nuclear membrane as the nucleus grows. This is consistent with what has been suggested experimentally [7]. Fig. 7A depicts how sensitively the result depends on the two parameters. Next we visually inspect the G3-A1 model predictions using the identified best parameters, Fig. 6B. We see that for most droplet sizes both the dynamics and the final time point behaviour is recapitulated by the model. However, we see a relatively large deviation between model and experiment for the three largest droplet sizes: The mean absolute error for those three is 16%, while it is 4.6% for the remaining 17 droplet sizes.

To assess the match between experimental measurements and simulation rate further, we return to the nuclear growth equation for G3 given in (23), assuming A1, i.e. $\kappa(R) \equiv k$. If we assume $R_0 = 0$ and $U_0 = \bar{u}\frac{4\pi R_c^3}{3}$, we obtain that

$$\frac{\mathrm{d}R}{\mathrm{d}t} = k\frac{\alpha\bar{u} - \left(\frac{R}{R_c}\right)^3}{1 - \left(\frac{R}{R_c}\right)^3},$$

i.e. the model predicts that if we normalize the nuclear radius by the droplet size, the rate of change in nuclear radius should fall on one common curve for all droplet sizes $r \mapsto k(\alpha\bar{u} - r^3)/(1 - r^3)$. To obtain a reliable estimates of $\dot{R}$ from the data, we fitted a smoothing spline through the time course data for each droplet size and evaluated the time derivative of its analytical representation at the original experimental time points (see Appendix D). Fig. 6E shows the comparison between theory and measurements. We can see that for most droplet sizes we obtain a good match between analytical prediction and experimental values. Only for very large droplet sizes ($67 - 78\mu m$) do nuclei grow slower than predicted. This is consistent with what we observed comparing Fig. 6A to 6B.

The approximate spatial model only improves the fit slightly. The well-mixed model is an approximation of the full model, valid in the limit $\varepsilon \to 0$, where $\varepsilon = \frac{R_c k}{D}$ for the G3-A1 model. This means that the approximation will be less good for larger droplet sizes R_c. For constant R_c and k we can also view the well-mixed model as a model obtained for infinitely fast diffusion. Thus, it is possible that for larger droplet sizes, nuclear growth will happen slower, since it takes some time until diffusion acts to redistribute NGF towards the nuclear membrane, where absorption reduces its availability.

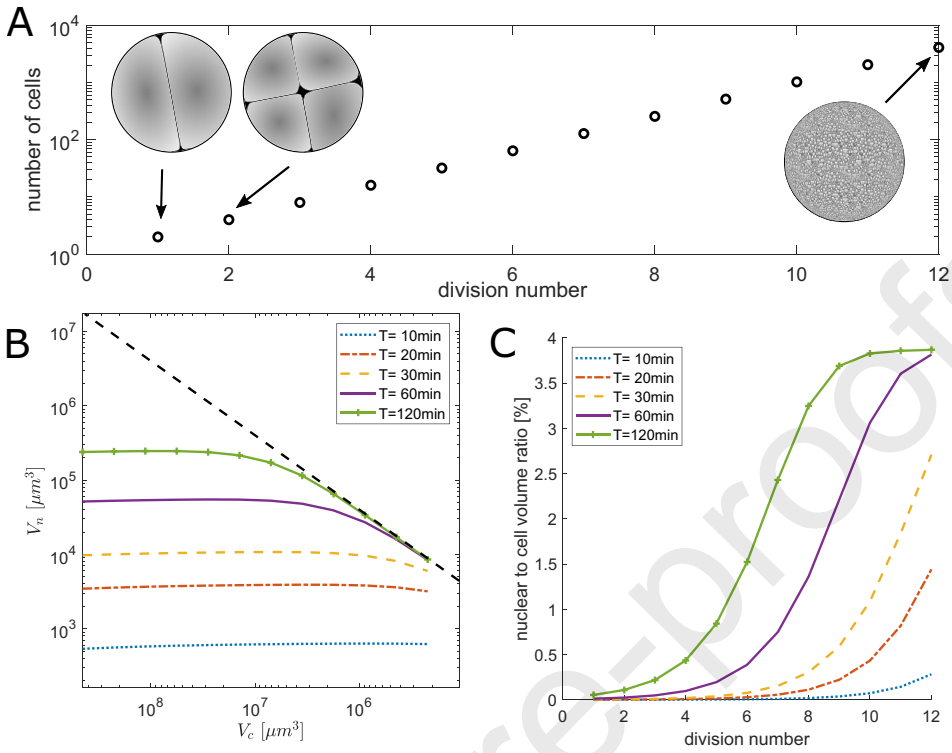

Figure 8: Nuclear scaling during early Xenopus development. A. Number of cells as function of division number. Schematics illustrate cells in embryo. B and C. Solutions of the G3-A1 full free boundary model for nuclear scaling. Shown is how nuclear volume V_n scales with cell volume V_c for different cell cycle lengths T. The dashed line in panel B represents the relationship for fully equilibrated nuclei, where $V_n = \alpha\bar{u}V_c$. Parameters used $\alpha\bar{u} = 0.04$, $k = 15\mu$m/min, $D = 300\mu$m^2/min. C. Nuclear to cell volume ratio as function of division number for the simulations in B.

To test this, we now use the approximate spatial model derived in Sec. 4 (reverting to physical dimensions). We now have three free parameters $\mathbf{p} = (\alpha\bar{u}, k, D)$, where D is the diffusion constant. Using the same error function, we repeat the parameter fitting procedure for G3-A1. The resulting best parameters are $\alpha = 0.0569$, $k = 4.44\mu$m/min and $D = 73\mu$m^2/min yielding a minimal average error of 5.7% per data point. Fig. 7B shows how sensitively the error depends on the three parameters. Using the approximate spatial model reduces the error by about 10%. Fig. 6C shows the nuclear growth prediction. We see that while allowing for finite diffusion slows the initial growth of nuclei in the very large droplets, measured nuclear size at the end of the observation interval is still smaller than the model predicts. Since the value for ε can reach up to around 5 for very large droplets, we also tested if we can obtain a better fit solving the full free boundary problem. However, this was not the case. The fact that nuclei in very large droplets grow slower than the model predicts might point to model limitations, discussed below.

6.2. Nuclear scaling in early development

Early Xenopus development. If cells divide rapidly before nuclear size can equilibrate, the time scale of nuclear growth plays a key role in understanding nuclear size. As an example, we use the model to explain nuclear scaling behaviour as observed in the literature during early Xenopus development. In the first few hours after fertilization, the Xenopus embryo (initially one cell of radius $\approx 600\mu$m) undergoes a rapid series of 12 synchronized cell divisions, taking around $15 - 30$min each and resulting in 4096 cells, Fig. 8A. Since the total volume stays the same, cells become progressively smaller [18]. In [17] the authors note that, while nuclei become smaller and

smaller with each subsequent division, they occupy a larger percentage of the cell. In light of our model, an intuitive explanation is that nuclear size takes longer to equilibrate in larger cells.

The model can recapitulate experimental behaviour. To test this, we use our nuclear scaling model. Since diffusion in the initially very large cells cannot be neglected, we solve the full free boundary problem, not one of its approximations. We set $\alpha\bar{u} = 0.04$, which corresponds to the karyoplasmic ratio measured in [17] at later stages and $D = 300\mu\text{m}^2/\text{min}$. Further $R_0 = 0$, since nuclei have to reform after each division. We assume the sum of all cell volumes stays constant and calculate the cell radius after the n-th division to be $R_c = 600 \times 2^{-n/3}\mu\text{m}$. We simulate the model for different values of cell cycle lengths (i.e. times between cell division) $T = 10, 20, 30, 60, 120\text{min}$. The result is depicted in Fig. 8B,C and recapitulates qualitatively the data in the first figure in [17]. As in their experiments, the karyoplasmic ratio increases as cells get smaller and plateaus at a value set by $\alpha\bar{u}$. Further, in our simulations we see that as the cell cycle length increases, nuclei become larger overall. However, this is much more pronounced for nuclei in larger cells than for those in smaller cells. This is because the latter are already close to their equilibrium size, even for short cell cycle lengths.

7. Model Limitations and Extensions

The presented model can be viewed as a minimal model that only includes the most important factors determining nuclear growth. In Sec. 6 we demonstrated that despite its simplicity the current model can explain experimental data. However, there are several limitations to this model and in this section we discuss how some effects could be included in this modelling framework. The below list is not exhaustive and any future model extension will be guided by experimental results.

Transport mechanism in the cytoplasm. In the current model we assume the transport of the NGF in the cytoplasm is purely diffusive, however other mechanisms might play a role. For instance there might be directed transport along microtubules. This would change the flux used in (1) from $\mathbf{J} = -D\nabla u$ to $\mathbf{J} = -D\nabla u + \mathbf{V}u$, where $\mathbf{V}$ is a vector valued function modelling the transport velocity along microtubules, that could depend on space and time. Different assumptions on microtubule density could be included. Microtubules are commonly found to be anchored at a microtubule organising center located at the nuclear membrane. In a first approximation one could therefore assume the transport happens radially, allowing to work with the radially symmetric model. We note that we expect the resulting well-mixed model to be the same as the one derived in this work. In general we expect that microtubule transport would not affect the limiting nuclear size, but rather the time scale to obtain it.

Modelling NPC dynamics. In Sec. 6 we observed that nuclear growth in large droplets (or cells) is slower than predicted by the model. A possible reason might be that the surface density of NPCs on the nuclear membrane is only constant for small to medium sized nuclei, but that NPC supply can become limiting for very large nuclear sizes. Here we suggest a simple model that would describe this behaviour: Let $N(t)$ be the number of NPCs on the nuclear surface at time t and $n(t) = N(t)/(4\pi R^2)$ the corresponding NPC surface density for a nucleus of radius R. We assume the NGF absorption rate κ is proportional to the NPC surface density $n(t)$. New NPCs need to be recruited from the cytoplasm, where their number is $M(t)$ and the total number of available NPCs is $N(t) + M(t) = M_0$. We assume there is a target NPC surface density $\bar{n}$ implying a nuclear size dependent target NPC number $4\pi R(t)^2\bar{n}$. If the recruitment rate to the nuclear membrane is proportional to how far the current NPC number is from the target NPC number, then we can write

$$\dot{N} = \eta\left(M_0 - N(t)\right)\left(4\pi R(t)^2\bar{n} - N(t)\right),$$

where η describes how fast NPC recruitment happens. It is easy to see that for η large and $4\pi R(t)^2 < M_0$, the NPC surface density remains roughly constant $n(t) \approx \bar{n}$, however for large

nuclear sizes, i.e. when $4\pi R(t)^2 > M_0$, we will have $n(t) \approx M_0/(4\pi R(t)^2)$, leading to a slowed down growth for very large nuclei. While this model extension would almost certainly lead to a better fit with the experimental data presented in Sec. 6, more experimental evidence is needed to confirm it is indeed NPC dynamics that slow the growth of very large nuclei.

Multiple nuclei. Multinucleated cells can be found in certain fungi [1], in developing organisms, e.g. the early drosophila [34] or also muscle cells [4]. In [35] it was observed that the sum of nuclear sizes within one cell scales linearly with cell size and that nuclei that are positioned further from other nuclei grow larger. This is consistent with what has been observed in [24] and the idea that nuclei that share a common cytoplasm compete for the NGF. Inclusion of several nuclei into the presented model is straightforward: For M nuclei the new cytoplasmic domain can be written as $\Omega(t) := \mathcal{C} \setminus \bigcup_{i=1}^{M} \mathcal{N}_i(t)$, where $\mathcal{N}_i$ denotes the space occupied by the i-th nucleus. The main NGF equation (1) then changes to

$$\begin{aligned} &\partial_t u = -\nabla \cdot \mathbf{J}, && \mathbf{x} \in \Omega(t) \\ &\mathbf{n} \cdot \mathbf{J} = 0 && \mathbf{x} \in \partial\mathcal{C}, \\ &\mathbf{n} \cdot \mathbf{J} = \kappa_i u + \mathbf{n} \cdot (u\mathbf{v}) && \mathbf{x} \in \partial\mathcal{N}_i(t), \end{aligned}$$

where the absorption rate κ_i can depend on the nucleus. This is complemented by the nuclear growth equations

$$\frac{\mathrm{d}}{\mathrm{d}t}\mathcal{Z}_i(t) = \alpha\kappa \int_{\partial\mathcal{N}_i(t)} u \,\mathrm{d}\Gamma,$$

where $\mathcal{Z}_i$, as previously, denotes some measure of nuclear size (radius, surface area or volume). In general there is no radially symmetry in this model, making both analysis and simulation more involved. However, in the simplified case of the well-mixed model, the position of the nuclei would not play a role and some insights about final nuclear sizes and time dynamics could be gained. For nuclei arranged linearly one could use cylindrical symmetry to derive a simplified model to analyse more deeply how nuclear position affects its size.

Nuclear export and shrinking. While the role of nuclear export in setting nuclear size is more unclear, the effects could be included in the current model. This would require posing a separate equation for the concentration (or number) of NGF inside the nucleus. Nuclear NGF can then either cause nuclear growth or be exported through NPCs. Further, instances of nuclear shrinking have also been reported and could be incorporated in future model developments [9].

Elastic Membrane. To incorporate the elastic nature of the nuclear envelope, and to describe non-spherical geometries associated with large deformations, the well-known Helfrich model [15] can be incorporated into our modeling framework. This approach is well established in modeling the dynamics of biological membrane structures [27] such as vesicles [29] or red blood cells [33].

Specifically, the elastic energy stored in the infinitesimally thin nuclear envelope $\partial\mathcal{N}$ takes the form

$$\mathcal{E}_B = \int_{\partial\mathcal{N}} 2\kappa_B(H - H_0)^2 dS + \int_{\partial\mathcal{N}} \kappa_K K dS, \qquad H = \frac{1}{2}(\kappa_1 + \kappa_2), \qquad K = \kappa_1\kappa_2,$$

where κ_1, κ_2 are the principle curvatures of the surface and H_0, κ_K, κ_B are quantities known as the spontaneous curvature, Gaussian modulus and bending modulus respectively [13]. Dynamics then arise from the minimization of this energy.

8. Discussion

Summary of work. In this work we derived and analysed a spatio-temporal mathematical model for nuclear growth based on the limiting component hypothesis. We used asymptotic techniques to

derive approximating models and tested their predictions against two different experimental setups. Comparing to time-dynamic experimental data, the computational model confirms that the prevalent scientific knowledge about nuclear growth also applies to our model system: That nuclear volume will be proportional to cell volume (G3) and that more NPCs are being incorporated into the nuclear membrane as it grows, keeping the NPC surface density relatively constant (A1). A constant karyoplasmic ratio has been observed in many species [5, 16]. That NPC surface density is constant across different nuclear sizes was also observed experimentally [31]. Finally our model also shows that the surprisingly slow growth of nuclei in very large droplets cannot be explained purely by diffusion-limited transport of NGF across the cell.

Discussion of parameters. From the parameter fitting we obtained the following biological parameters from the G3-A1 model: $\alpha\bar{u} \approx 0.05$-$0.07$ of $k \approx 2.5$-5μm/min and possibly $D \approx 50$-$100\mu\text{m}^2$/min. For *de nuovo* growth, the parameter combination $\alpha\bar{u}$ sets the karyoplasmic ratio V_n/V_c. As necessary to avoid nuclei reaching cell size, it is less than 1. Experimentally, one could test whether reduction of $\bar{u}$, e.g. by dilution of the Xenopus extract leads to a corresponding reduction in equilibrium nuclear size. Next, the absorption rate $\kappa = k$ is the product between the NPC density on the nuclear surface and the processing power per NPC. Experimentally NPC surface density has been measured to be between 5 and 10 NPCs/μm^2 [31, 21], hence our results suggest a processing power of around 0.25-1 molecules NGF imported per NPC per minute per molecule NGF present in one cubic micrometer. In the future we plan to measure and manipulate import rates and compare them to the model predictions. The obtained diffusion constant, while within realistic biological ranges, is relatively small compared to what we would expect: E.g. for a 50kDa molecule diffusing in Xenopus extract (dynamic viscosity of $\eta \approx 20$mPa-s [32]), we'd expect around $260\mu\text{m}^2$/min at room temperature. It is of course possible that the molecule in question is in fact larger, however it seems more likely that the result points towards model limitations. In Sec. 7 we discussed model extension concerning different transport mechanism via microtubules and incorporating time depdendent NPC dynamics, which could explain the slowed down nuclear growth in large cells.

Regulation and function of nuclear size. Changes in karyoplasmic ratio (both larger and smaller) have been associated to different types of cancer [28] and both Lamins and NPCs have been implicated [30]. In this model we assumed there is only one NGF that dominates nuclear size determination. However, in reality there are more likely a number of such factors. Which of those factor is limiting and hence sets nuclear size can vary between organisms, cell type, cell cycle, disease state, etc. Future computational models should allow for this complexity as well as incorporate other suggested transport mechanisms of NGFs across the cytoplasm. Further, there are still open questions regarding the function of nuclear size scaling. Commonly DNA copy number is not affected by size scaling (however, there are exceptions, see e.g. [35])), however DNA organisation and processing is affected by nuclear scaling [22]. Hence a larger nucleus can produce more mRNA and has a larger surface area through which mRNA can be exported. Exploring this relationship between nuclear size and nuclear product production and transport using experimental and computational tools will be an important task for future work.

References

[1] Alberti-Segui, C., Dietrich, F., Altmann-Johl, R., Hoepfner, D., and Philippsen, P. (2001). Cytoplasmic dynein is required to oppose the force that moves nuclei towards the hyphal tip in the filamentous ascomycete ashbya gossypii. *Journal of Cell Science*, 114(5):975–986.

[2] Baetcke, K., Sparrow, A., Nauman, C., and Schwemmer, S. S. (1967). The relationship of dna content to nuclear and chromosome volumes and to radiosensitivity (ld50). *Proceedings of the National Academy of Sciences of the United States of America*, 58(2):533.

[3] Bernoff, A. J. and Lindsay, A. E. (2018). Numerical approximation of diffusive capture rates by planar and spherical surfaces with absorbing pores. *SIAM J. Applied Math.*, 78(1):266–290.

[4] Bruusgaard, J., Liestøl, K., Ekmark, M., Kollstad, K., and Gundersen, K. (2003). Number and spatial distribution of nuclei in the muscle fibres of normal mice studied in vivo. *The Journal of Physiology*, 551(2):467–478.

[5] Chan, Y.-H. M. and Marshall, W. F. (2010). Scaling properties of cell and organelle size. *Organogenesis*, 6(2):88–96. PMID: 20885855.

[6] Chen, P., Tomschik, M., Nelson, K., Oakey, J., Gatlin, J. C., and Levy, D. L. (2019). Cytoplasmic volume and limiting nucleoplasmin scale nuclear size during xenopus laevis development. *Development*.

[7] D'angelo, M. A., Anderson, D. J., Richard, E., and Hetzer, M. W. (2006). Nuclear pores form de novo from both sides of the nuclear envelope. *Science*, 312(5772):440–443.

[8] Desai, A., Murray, A., Mitchison, T. J., and Walczak, C. E. (1999). The use of xenopus egg extracts to study mitotic spindle assembly and function in vitro. *Methods in Cell Biology*, 61:385.

[9] Edens, L. J. and Levy, D. L. (2014). cpkc regulates interphase nuclear size during xenopus development. *Journal of Cell Biology*, 206(4):473–483.

[10] Gatlin, J. C., Matov, A., Groen, A. C., Needleman, D. J., Maresca, T. J., Danuser, G., Mitchison, T. J., and Salmon, E. D. (2009). Spindle fusion requires dynein-mediated sliding of oppositely oriented microtubules. *Current Biology*, 19(4):287–296.

[11] Gregory, T. R. (2005). Genome size evolution in animals. In *The Evolution of the Genome*, pages 3–87. Elsevier.

[12] Gu, Y., Yam, C., and Oliferenko, S. (2012). Divergence of mitotic strategies in fission yeasts. *Nucleus*, 3(3):220–225.

[13] Guckenberger, A. and Gekle, S. (2017). Theory and algorithms to compute helfrich bending forces: a review. *Journal of Physics: Condensed Matter*, 29(20):203001.

[14] Hara, Y. and Merten, C. A. (2015). Dynein-based accumulation of membranes regulates nuclear expansion in xenopus laevis egg extracts. *Developmental Cell*, 33(5):562–575.

[15] Helfrich, W. (1973). Elastic properties of lipid bilayers: Theory and possible experiments. *Z. Naturforsch.*, 28(11-12):693–703.

[16] Huber, M. D. and Gerace, L. (2007). The size-wise nucleus: nuclear volume control in eukaryotes. *The Journal of Cell Biology*, 179(4):583–584.

[17] Jevtić, P. and Levy, D. L. (2015). Nuclear size scaling during xenopus early development contributes to midblastula transition timing. *Current Biology*, 25(1):45–52.

[18] Jones, C. M. and Smith, J. C. (2008). An overview of xenopus development. *Molecular Embryology*, pages 385–394.

[19] Jorgensen, P., Edgington, N. P., Schneider, B. L., Rupeš, I., Tyers, M., and Futcher, B. (2007). The size of the nucleus increases as yeast cells grow. *Molecular Biology of the Cell*, 18(9):3523–3532.

[20] Kleiber, M. (1947). Body size and metabolic rate. *Physiological Reviews*, 27(4):511–541.

[21] Levy, D. L. and Heald, R. (2010). Nuclear size is regulated by importing α and ntf2 in xenopus. *Cell*, 143(2):288–298.

[22] Levy, D. L. and Heald, R. (2012). Mechanisms of intracellular scaling. *Annual Review of Cell and Developmental Biology*, 28(1):113–135. PMID: 22804576.

[23] Lindsay, A. E., Bernoff, A. J., and Ward, M. J. (2017). First passage statistics for the capture of a brownian particle by a structured spherical target with multiple surface traps. *Multiscale Modeling and Simulation*, 15(1):74–109.

[24] Neumann, F. R. and Nurse, P. (2007). Nuclear size control in fission yeast. *The Journal of Cell Biology*, 179(4):593–600.

[25] Newport, J. W., Wilson, K. L., and Dunphy, W. G. (1990). A lamin-independent pathway for nuclear envelope assembly. *The Journal of Cell Biology*, 111(6):2247–2259.

[26] Oakey, J. and Gatlin, J. C. (2018). Microfluidic encapsulation of demembranated sperm nuclei in xenopus egg extracts. *Cold Spring Harbor Protocols*, 2018(8).

[27] Rangamani, P., Benjamini, A., Agrawal, A., Smit, B., Steigmann, D. J., and Oster, G. (2014). Small scale membrane mechanics. *Biomech Model Mechanobiol*, 13(4):697–711.

[28] Rizzotto, A. and Schirmer, E. C. (2017). Breaking the scale: how disrupting the karyoplasmic ratio gives cancer cells an advantage for metastatic invasion. *Biochemical Society Transactions*, 45(6):1333–1344.

[29] Ruiz-Herrero, T., Fai, T. G., and Mahadevan, L. (2019). Dynamics of growth and form in prebiotic vesicles. *Phys. Rev. Lett.*, 123:038102.

[30] Simon, D. N. and Rout, M. P. (2014). Cancer and the nuclear pore complex. *Cancer Biology and the Nuclear Envelope*, pages 285–307.

[31] Theerthagiri, G., Eisenhardt, N., Schwarz, H., and Antonin, W. (2010). The nucleoporin nup188 controls passage of membrane proteins across the nuclear pore complex. *Journal of Cell Biology*, 189(7):1129–1142.

[32] Valentine, M., Perlman, Z., Mitchison, T., and Weitz, D. (2005). Mechanical properties of xenopus egg cytoplasmic extracts. *Biophysical Journal*, 88(1):680–689.

[33] Vlahovska, P. M., Podgorski, T., and Misbah, C. (2009). Vesicles and red blood cells in flow: From individual dynamics to rheology. *Comptes Rendus Physique*, 10(8):775–789. Complex and biofluids.

[34] Warn, R. (1986). The cytoskeleton of the early drosophila embryo. *Journal of Cell Science*, 1986(Supplement_5):311–328.

[35] Windner, S. E., Manhart, A., Brown, A., Mogilner, A., and Baylies, M. K. (2019). Nuclear scaling is coordinated among individual nuclei in multinucleated muscle fibers. *Developmental Cell*, 49(1):48–62.

Appendix A. Experimental Material and Methods

Nuclear assembly in Xenopus egg extracts. Cytostatic factor (CSF)-arrested egg extracts were prepared as described previously [8]. Interphase extract was maintained by the addition of calcium and cycloheximide. De-membranated sperm nuclei were prepared as described previously (Hazel and Gatlin, 2018) and fluorophores were subsequently added to the prepared extract, which was immediately loaded into microfluidic devices (see below for details). GFP-NLS was added to the extract at a final concentration of 2μM to visualize nuclear import. The standard nuclear assembly reaction was 100μl fresh extract, 0.4mM CaCl2, 100μg/ml cycloheximide and 1000 Xenopus sperm nuclei per μl. Reactions were incubated at 16-18°C and spherical, import- competent nuclei generally formed within 30-45min.

Microfluidic device fabrication and encapsulation of Xenopus egg extract. Microfluidic devices were prepared essentially as described in [26]. Briefly, devices were cast in polydimethylsiloxane (PDMS, Sylgard 184, Dow Corning) using well-established soft lithography techniques. A microchannel network was designed in AutoCAD (Autodesk, Inc) drafting software. The photomask was output to film (CAD/Art Services, Bandon, OR) and used to lithographically expose the network in a photoresist film (SU-3025, MicroChem, Newton, MA) spun onto a silicon wafer at 30µm. Polydimethylsiloxane (PDMS) elastomer was then poured over the patterned wafer, cured at 70°C, and removed, producing an imprinted channel network. Fluid inlet and outlet ports were punched into the PDMS with a sharpened, unbeveled syringe tip (Brico Medical, Dayton, NJ). The PDMS channel network was exposed to oxygen plasma (Harrick Plasma, Ithaca, NY) and placed in contact with a cover glass slip (#1.5, Thomas Scientific) to form an irreversible bond.

Imaging and nuclear size measurements. Images were acquired in the Gatlin lab using either a scientific-grade CMOS camera (Orca Flash 2.8, Hamamatsu) mounted on an inverted epifluorescence microscope (IX71 stand, Olympus) or an EM-CCD camera (ImagEM, Hamamatsu) mounted on an IX71 stand equipped with a spinning-disc confocal head (CSU- X1; Yokogawa). Confocal illumination was provided by an LMM5 laser launch (Spectral Applied research). Integration of all imaging systems components was provided by Biovision Technologies (Exton, PA). All image acquisition and analysis was performed using Metamorph 7.7 software (Molecular Devices). Images were acquired using Olympus objectives of varying magnification: 10x (0.24 NA), 20x (0.75 NA and 0.85 NA), 40x (1.30 NA), and 60x (1.49 NA).

Some images were also acquired using microscopes at the Marine Biological Laboratory (MBL). This included a Nikon Ti-E fully motorized microscope with perfect focus (PFS3), encoded motorized XY stage, Plan Apo Lambda 10x 0.45 N.A., 20x 0.75 N.A., 40x 0.95 N.A., 60x 1.40N.A. oil, 100x 1.45 N.A. oil objectives, LU-NV laser combiner (405nm, 445nm, 488nm, 515nm, 561nm, 647nm), Intensilight epi-fluorescence light source, NIS-Elements AR software (Nikon Instruments, Inc.) with Yokogawa CSU X1 5000 RPM spinning disc confocal (Solamere Technology), 6-position triggered emission wheel (Finger Lakes Inc.), iXon Ultra EM-CCD detector (Andor) for the SDC lightpath and DS-Qi2 CMOS camera (Nikon Instruments) for the epi light path, 35mm Smart shutters for transmitted and epi-fluorescence (Sutter), Nano-Z100-N piezo-z stage (Mad City Labs). We also used a wide-field system at the MBL. Here, images were acquired using a Nikon Ti-E fully motorized microscope with perfect focus (PFS3), encoded motorized XY stage, Plan Apo Lambda 10x 0.45 N.A., 20x 0.75 N.A., 40x 0.95 N.A., 60x 1.40 N.A. oil, 100x 1.45 N.A. oil objectives with DIC optics, HiSN Zero shift filter cubes for DAPI, GFP, TxRed and Cy5, Intensilight epi-fluorescence light source, DS-Qi2 CMOS camera, NIS-Elements AR software (Nikon Instruments, Inc.) with 35mm Smart shutters for transmitted and epi-fluorescence (Sutter).

Measurements of Nuclear Size. Multi-dimensional z-stack imaging of encapsulated nuclei allowed precise determination of encapsulating droplet diameter and the maximum nuclear cross section (as determined by GFP-NLS labeling). For control reactions, nuclei were assembled in unconfined extracts at a concentration of 150 nuclei/µl and fixed every 15 minutes (beginning at t=30min) in 4µl of extract was fixed by addition of 16µl of spindle fix with DAPI [8]. This is a concentration at which cytoplasmic components should not be limited in bulk extract, allowing unbounded nuclear growth over the time periods relevant to this study (see Figure 2A; [14]). To avoid altering nuclear morphology, imaging of fixed nuclei was carried out in micromanipulation chambers [10]. 25µm^2 coverslips were used to cover circular cutouts in custom-made metal slides. 8µl of fixed nuclei were spread out on the coverslip and overlaid with 200µl of mineral oil.

Maximum nuclear cross-sectional areas were measured from thresholded 3-D image stacks in ImageJ and used to calculate nuclear surface area and volume assuming a spherical nucleus. For this reason, only largely spherical nuclei (those with a spherical form factor of 0.75-1 as calculated by ImageJ) were subjected to analysis.

Appendix B. Compressible Cytoplasm

General Model. If the NGF moves mainly with the (compressible) immersed structures in the cytoplasm, we assume nuclear growth leads to movement of the material points throughout the cytoplasm in a continuous manner. In this case $\mathbf{v}$ is continuous inside the domain. Then we obtain

$$\begin{aligned} &\partial_t u + \nabla \cdot (u\mathbf{v}) = -\nabla \cdot \mathbf{J}, \qquad x \in \Omega(t) \\ &\mathbf{n} \cdot \mathbf{J} = 0 \qquad \mathbf{x} \in \partial\mathcal{C}, \\ &\mathbf{n} \cdot \mathbf{J} = \kappa u \qquad \mathbf{x} \in \partial\mathcal{N}(t). \end{aligned} \tag{B.1}$$

At the cell membrane $\mathbf{v} = 0$, since it is modelled as impenetrable. At the nuclear membrane we again assume that $\mathbf{v} = -\mathbf{n}\dot{R}$. In between $\mathbf{v}$ is a continuous function of the position $\mathbf{x}$ and we will suggest a definite shape below. Analogously to the incompressible model, we can derive the total NGF balance (2).

Radially symmetric cell. Using the same assumptions as in Sec. 3, we can simplify (B.1) to

$$\begin{aligned} &\partial_t u + \frac{1}{r^2}\partial_r \left(r^2 v(r,t) u\right) = D\frac{1}{r^2}\partial_r \left(r^2 \partial_r u\right), \quad R(t) < r < R_c; \\ &D\partial_r u = 0, \quad r = R_c; \\ &D\partial_r u = \kappa u, \quad r = R(t). \end{aligned} \tag{B.2}$$

We need to specify the material point velocity $v(r,t)$ which we require to fulfil $v(R(t),t) = \dot{R}(t)$ and $v(R_c,t) = 0$. Different models are possible, but here we assume the compression to be uniform, i.e. the density of cytoplasmic material will stay spatially constant. This yields the following material point velocity

$$v(r,t) = \dot{R}(t)\left(\frac{R(t)}{r}\right)^2 \frac{R_c^3 - r^3}{R_c^3 - R(t)^3}. \tag{B.3}$$

Since $R(t) < R_c$, v decreases as a function of r. This is due to the fact that maintaining a constant cytoplasmic density in a spherical geometry requires cytoplasmic material to be pushed outwards faster near the center than at distal portions of the cell. To show that this material point velocity indeed leads to a uniform density upon compression, we consider a transport equation in spherical coordinates for the radially symmetric cytoplasmic density $\rho(r,t)$

$$\partial_t \rho + \frac{1}{r^2}\partial_r \left(r^2 v(r) \rho\right) = 0,$$

with v given by (B.3) and an initial spatially uniform density $\rho(r,0) = \rho_0$. In the following we define $R_0 = R(0)$. It is easy to check that the solution is given by the spatially constant density

$$\rho(r,t) = \rho(t) = \rho_0 \frac{R_c^3 - R_0^3}{R_c^3 - R(t)^3}.$$

Finally, to confirm that total mass is conserved, we multiply this density by the volume of the cytoplasm at time t, we find the total mass at time t, which is

$$\rho_0 \frac{R_c^3 - R_0^3}{R_c^3 - R(t)^3} \times \frac{4\pi}{3}\left(R_c^3 - R(t)^3\right) = \rho_0 \frac{4\pi}{3}\left(R_c^3 - R_0^3\right),$$

which is independent of time.

Appendix C. Asymptotics

In this section we develop the solution of (11) in terms of the regular expansion

$$u = u^0 + \varepsilon u^1 + \mathcal{O}(\varepsilon^2), \qquad R(t) = R^0(t) + \varepsilon R^1(t) + \mathcal{O}(\varepsilon^2). \tag{C.1}$$

Expanding the boundary condition (11b) yields that $\partial_r u^j = 0$ on $r = 1$ for $j = 0, 1, 2, \ldots$. On the boundary $r = R(t)$, the expansion of the left hand side of (11c) takes the form

$$\begin{aligned}\partial_r u(R(t), t) &= \partial_r u^0(R(t), t) + \varepsilon\, \partial_r u^1(R(t), t) + \mathcal{O}(\varepsilon^2) \\ &= \partial_r u^0\Big|_{r=R^0} + \varepsilon\Big[R^1 \partial_r^2 u^0 + \partial_r u^1\Big]_{r=R^0} + \mathcal{O}(\varepsilon^2)\end{aligned}$$

The right hand side of (11c) expands as

$$\varepsilon\big[\kappa(R) - \dot{R}\big]u = \varepsilon\left[\kappa - \dot{R}^0\right]u^0\Big|_{r=R^0} + \mathcal{O}(\varepsilon^2). \tag{C.2}$$

Expanding (12) the nuclear growth equation $\frac{d}{dt}[z(R)] = aR^2\kappa u$ reveals that

$$\frac{\mathrm{d}}{\mathrm{d}t}\left(z(R^0) + \varepsilon z'(R^0)R^1 + \mathcal{O}(\varepsilon^2)\right) = -a\left(\frac{\mathrm{d}U^0}{\mathrm{d}t} + \varepsilon\frac{\mathrm{d}U^1}{\mathrm{d}t} + \mathcal{O}(\varepsilon^2)\right) \tag{C.3a}$$

while simultaneously we have that

$$\frac{d}{dt}[z(R)] = a(R^0)^2\kappa u^0\Big|_{r=R^0} + a\,\varepsilon\Big((R^0)^2\kappa u^1 + 2R^0R^1\kappa\, u^0 + R^1(R^0)^2\kappa' u^0\Big)\Big|_{r=R^0} + \mathcal{O}(\varepsilon^2). \tag{C.3b}$$

Comparing (C.3a) and (C.3b), we have that

$$\frac{\mathrm{d}}{\mathrm{d}t}(z(R^0)) = a(R^0)^2\kappa u^0\Big|_{r=R^0}, \tag{C.4a}$$

$$\frac{\mathrm{d}}{\mathrm{d}t}(z'(R^0)R^1) = -a\frac{\mathrm{d}U^1}{\mathrm{d}t} = a\Big((R^0)^2\kappa u^1 + 2R^0R^1\kappa u^0 + R^1(R^0)^2\kappa' u^0\Big)\Big|_{r=R^0}. \tag{C.4b}$$

Incorporating these expansions of the boundary terms and the NGF rate, we sequentially formulate problems for (u^j, R^j) for $j = 0, 1$.

$\underline{\mathcal{O}(\varepsilon^0)}$: The problem for (u^0, R^0) satisfies

$$0 = \frac{1}{r^2}\partial_r\left(r^2\partial_r u^0\right), \qquad R^0 < r < 1, \quad t > 0; \tag{C.5a}$$

$$\partial_r u_0^0 = 0, \qquad r = 1, \qquad t > 0; \tag{C.5b}$$

$$\partial_r u_0^0 = 0, \qquad r = R^0, \qquad t > 0; \tag{C.5c}$$

$$\frac{\mathrm{d}}{\mathrm{d}t}\left(z(R^0)\right) = a\kappa(R^0)(R^0)^2u^0\,. \tag{C.5d}$$

The solution of problem (C.5) is a time dependent constant $u^0(r, t) := u^0(t)$. To fix the value of this constant, we proceed to the correction term.

$\underline{\mathcal{O}(\varepsilon^1)}$: The problem for (u^1, R^1) satisfies

$$\frac{\mathrm{d}u^0}{\mathrm{d}t} = \frac{1}{r^2}\partial_r(r^2\partial_r u^1), \qquad R^0 < r < 1, \quad t > 0; \tag{C.6a}$$

$$\partial_r u^1 = 0, \qquad r = 1, \qquad t > 0; \tag{C.6b}$$

$$\partial_r u^1 = u^0(\kappa(R^0) - \dot{R}^0), \qquad r = R^0(t), \qquad t > 0; \tag{C.6c}$$

$$\frac{\mathrm{d}}{\mathrm{d}t}\left(z'(R^0)R^1\right) = -a\frac{\mathrm{d}U^1}{\mathrm{d}t}. \tag{C.6d}$$

Integrating (C.6a) over $(R^0, 1)$ and applying the boundary conditions (C.6b-C.6c) fixes the dynamics of $u^0(t)$. Together with the growth equation (C.5d), and suitable initial conditions, we have that

$$\frac{\mathrm{d}u^0}{\mathrm{d}t} = -\frac{(R^0)^2}{W} u^0(R^0)\left(\kappa(R^0) - \dot{R}^0\right), \qquad u^0(0) = u_0 \tag{C.7a}$$

$$\frac{\mathrm{d}}{\mathrm{d}t}\left(z(R^0)\right) = a\kappa(R^0)(R^0)^2 u^0, \qquad R^0(0) = r_0. \tag{C.7b}$$

where

$$W = \int_{R^0}^1 r^2 \,\mathrm{d}r = \frac{1-(R^0)^3}{3},$$

is a measure of the cytoplasmic volume. To fully specify the correction, we proceed from (C.6) by integrating (C.6a) to obtain that

$$u^1 = \frac{\mathrm{d}u^0}{\mathrm{d}t} g(r) + C,$$

for constant C and $g(r) = (r^3+2)/(6r)$. Here $g(r)$ can be identified as the Green's function for the Laplacian with the source at the origin. It then follows that

$$\int_{R^0}^1 u^1 r^2 \,\mathrm{d}r = \frac{\mathrm{d}u^0}{\mathrm{d}t} \int_{R^0}^1 g(r) r^2 \,\mathrm{d}r + C \int_{R^0}^1 r^2 \,\mathrm{d}r,$$

so that the constant C can be identified as

$$C = \frac{1}{W}\left(U^1 + R^1 (R^0)^2 u^0 - \frac{\mathrm{d}u^0}{\mathrm{d}t} \int_{R^0}^1 g(r) r^2 \,\mathrm{d}r\right), \qquad U^1 = \int_{R^0}^1 u^1 r^2 \,\mathrm{d}r - R^1 (R^0)^2 u^0.$$

The final form of first order correction u^1 is

$$u^1(r,t) = \frac{\mathrm{d}u^0}{\mathrm{d}t}\left(g(r) - \frac{1}{W}\int_{R^0}^1 g(r) r^2 \,\mathrm{d}r\right) + \frac{1}{W}\left(U^1 + R^1 (R^0)^2 u^0\right). \tag{C.8}$$

In combination with the rate equations (C.6d) and (C.4b), and suitable initial conditions, we find the time dependent constants $(R^1(t), U^1(t))$ satisfy

$$\frac{\mathrm{d}U^1}{\mathrm{d}t} = -\left((R^0)^2 \kappa u^1 + 2R^0 R^1 \kappa u^0 + R^1 (R^0)^2 \kappa' u^0\right)\Big|_{r=R^0}, \qquad U^1(0) = 0. \tag{C.9a}$$

$$\frac{\mathrm{d}}{\mathrm{d}t}\left(z'(R^0) R^1\right) = -a\frac{\mathrm{d}U^1}{\mathrm{d}t}, \qquad R^1(0) = 0. \tag{C.9b}$$

Appendix D. Numerical Methods

Simulation of full PDE. In order to simulate the full PDE given by (5) and (9), which is posed on a moving domain $r \in [R(t), R_c]$, we transform it onto a stationary domain using the change of variables $s = \frac{r-R(t)}{R_c - R(t)}$, $s \in [0,1]$. We let $u(r,t) = \hat{u}(s,t)$, then (5) and (9) become

$$\frac{\partial \hat{u}}{\partial t} + \frac{\dot{R}(s-1)}{R_c - R}\frac{\partial \hat{u}}{\partial s} = \frac{D}{(R_c - R)^2 (s(R_c - R) + R)^2}\frac{\partial}{\partial s}\left((s(R_c - R) + R)^2 \frac{\partial \hat{u}}{\partial s}\right),$$

$$\frac{\partial \hat{u}}{\partial s} = 0, \qquad s = 1,$$

$$D\frac{1}{R_c - R}\frac{\partial \hat{u}}{\partial s} = (\kappa - \dot{R})\hat{u}, \qquad s = 0,$$

$$\frac{\mathrm{d}}{\mathrm{d}t}(z(R)) = 4\pi\alpha\kappa(R) R^2 \hat{u}(0,t), \qquad R(0) = R_0.$$

To discretise the PDE we let the timestep be Δt and the spatial step be Δs, so we can define $t_m = m\Delta t$, $s_n = n\Delta s$, $u_m^n = \hat{u}(s_n, t_m)$ and $R_m = R(t_m)$, with $n = 0, 1, ..., N$, $m = 0, 1, ..., M$. We discretise the PDE using a first order backwards finite difference for the time derivative, which makes our numerical method implicit. A central difference discretisation is used for the first order spatial derivative. We discretize the flux term as follows:

$$\begin{aligned}\frac{\partial}{\partial s}\left(a(s)\frac{\partial \hat{u}}{\partial s}\right) &\approx \frac{a_{i+1/2}\frac{\partial}{\partial s}(u_{i+1/2}) - a_{i-1/2}\frac{\partial}{\partial s}(u_{i-1/2})}{\Delta s} \\ &\approx \frac{(a_i + a_{i+1})(u_{i+1} - u_i) - (a_i + a_{i-1})(u_i - u_{i-1})}{2\Delta s^2}\end{aligned}$$

To deal with the non-linear boundary condition at $s = 0$, we make an approximation where one u is evaluated at the previous time step, as shown below. Together this yields the following:

$$\begin{aligned}&\frac{u_m^n - u_{m-1}^n}{\Delta t} + \frac{(s_n - 1)\dot{R}_m}{R_c - R_m}\frac{u_m^{n+1} - u_m^{n-1}}{2\Delta s} \\ &= \frac{D}{(R_c - R_m)^2 (r_m^n)^2}\left[\frac{((r_m^n)^2 + (r_m^{n+1})^2)(u_m^{n+1} - u_m^n) - ((r_m^n)^2 + (r_m^{n-1})^2)(u_m^n - u_m^{n-1})}{2\Delta s^2}\right],\end{aligned}$$

where we define

$$r_m^n = (R_c - R_m)s_n + R_m.$$

For the boundary conditions we use

$$\begin{aligned}u_m^N - u_m^{N-1} &= 0, \\ \frac{D}{R_c - R_m}\frac{u_m^1 - u_m^0}{\Delta s} &= (\kappa - d\hat{R}_m)u_m^1,\end{aligned}$$

where we define

$$d\hat{R}_m = \frac{4\pi\alpha\kappa(R_m)R_m^2 u_m^0}{z'(R_m)}.$$

Finally, for the nuclear growth equation we use

$$\frac{R_m - R_{m-1}}{\Delta t} = \frac{4\pi\alpha\kappa(R_{m-1})R_{m-1}^2 u_{m-1}^0}{z'(R_{m-1})}.$$

We note that a constant-in-space initial signal concentration u_0 does not fulfill the boundary conditions, so we run the simulation for a few time steps to create an initial signal concentration that fulfils the boundary conditions, and then re-scale such that the average initial signal concentration is equal to u_0.

Simulation of approximate models. To simulate the coupled ODEs for the asymptotic approximation, we use the built in MATLAB solver ode45 which is based on an explicit Runge-Kutta method.

Approximation of derivative of experimental data. In Sec. 6 we use an approximation of the time derivative of the experimentally measured nuclear growth data. We do this by fitting a smoothing spline through each set of time dependent nuclear growth measurements. A smoothing spline minimises a linear combination between the squared distance between measurements and the spline, and the integral of the square of the second derivative of the the spine with weights p and $1 - p$ respectively. We used $p = 0.0005$. We then use the exact time derivative of the resulting smoothing spline.

Appendix E. Experimental Data

Fig. Appendix E shows the experimental data used in Sec. 6. Each subplot represents the nuclear size as a function of time measured in droplets of varying diameter. For each data point between 13 and 195 individual measurements were made.

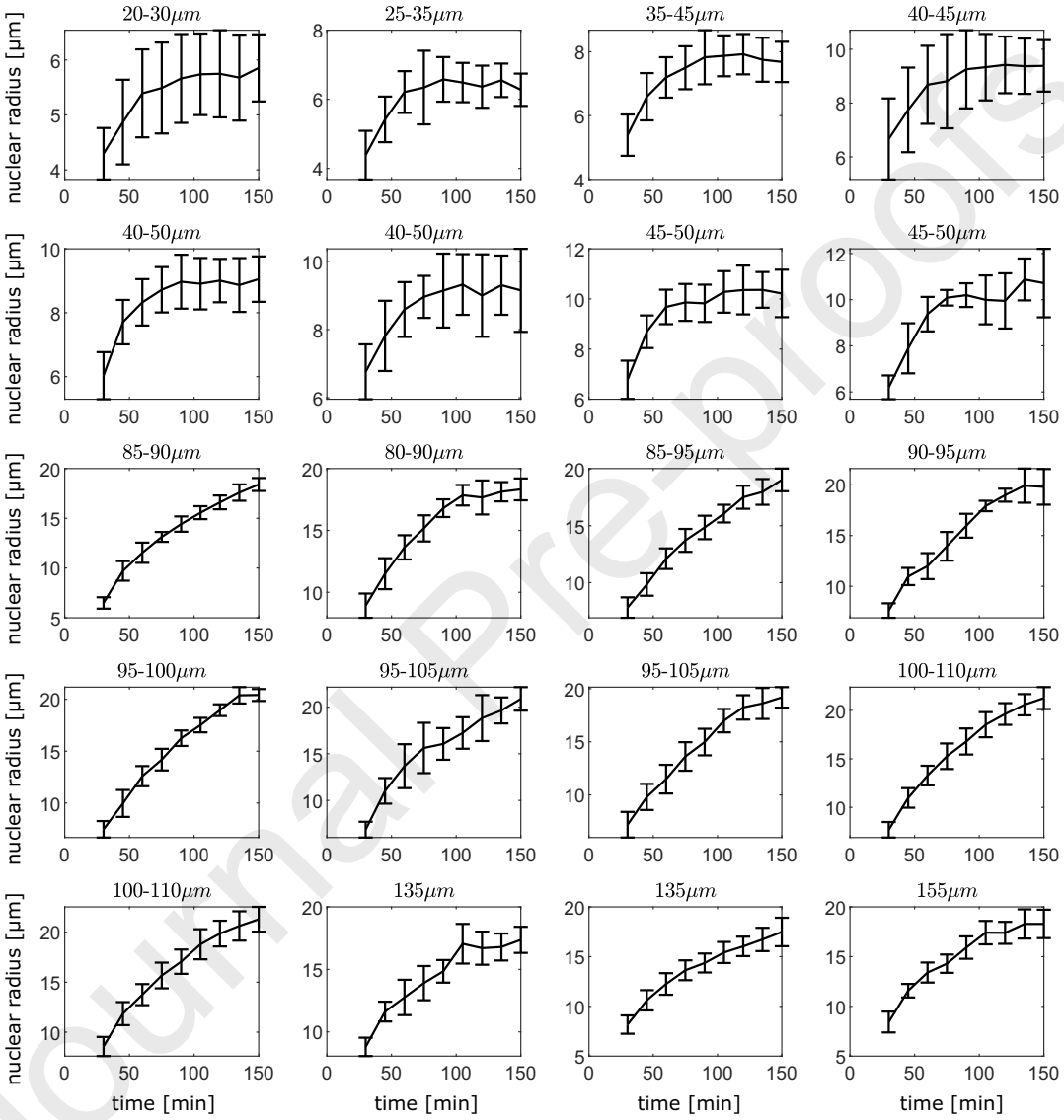

Figure E.9: Experimental data. Nuclear growth data obtained as described in Appendix A and used in Sec. 6. For each subplot the title denotes the diameter range of the droplets used. Error bars denote mean and standard deviation.